INTERNATIONAL JOURNAL FOR NUMERICAL METHODS IN FLUIDS
*Int. J. Numer. Meth. Fluids* 2005; **48**:1067–1099
Published online 7 April 2005 in Wiley InterScience (www.interscience.wiley.com). DOI: 10.1002/fld.961

# Large eddy simulation of turbulent incompressible flows by a three-level finite element method

Volker Gravemeier[1,2,*,†], Wolfgang A. Wall[2,‡] and Ekkehard Ramm[3,§]

[1]*Center for Turbulence Research, Stanford University, Stanford, CA 94305, U.S.A.*
[2]*Chair for Computational Mechanics, Technical University of Munich, Boltzmannstraße 15, D-85747 Garching, Germany*
[3]*Institute of Structural Mechanics, University of Stuttgart, Pfaffenwaldring 7, D-70550 Stuttgart, Germany*

SUMMARY

The variational multiscale method provides a methodical framework for large eddy simulation of turbulent flows. In this work, a particular implementation in the form of a three-level finite element method separating large resolved, small resolved, and unresolved scales is proposed. Residual-free bubbles are used for the numerical approximation of the small-scale momentum equation. A stabilizing term is added, in order to take into account the effect of the small-scale continuity equation. This implementation guarantees the stability of the method without further provisions and offers substantial computational savings on the small-scale level. Furthermore, it is accounted for the unresolved scales by a specific dynamic modelling procedure. The method is tested for two different turbulent flow situations. Copyright © 2005 John Wiley & Sons, Ltd.

KEY WORDS: large eddy simulation; variational multiscale method; three-level finite element method; dynamic subgrid-scale modelling; residual-free bubbles

## 1. INTRODUCTION

Incompressible flow is mathematically specified by the incompressible version of the set of Navier–Stokes equations. They are basically valid for both laminar and turbulent flow, although these flow states are quite different from a physical point of view. The occurrence of one or the other state strongly depends on the Reynolds number associated with the flow. In typical engineering applications, turbulent flows are surely prevalent due to their positive features like, for instance, a more effective transport and mixing ability with respect to a comparable laminar flow. The straightforward approach for a numerical solution of a turbulent flow called direct

*Correspondence to: Volker Gravemeier, Chair for Computational Mechanics, Technical University of Munich, Boltzmannstraße 15, D-85747 Garching, Germany.
† E-mail: vgravem@lnm.mw.tum.de
‡ E-mail: wall@lnm.mw.tum.de
§ E-mail: eramm@statik.uni-stuttgart.de

*Received 29 October 2004*
*Revised 10 December 2004*
*Accepted 20 December 2004*

numerical simulation (DNS), i.e. simply solving the Navier–Stokes equations numerically with full resolution and appropriate boundary conditions, reaches its limitations soon. Lowering the demands of resolution leads to what is established under the name 'large eddy simulation' (LES) in the meantime. See, for example, Reference [1] for a comprehensive overview. LES aims at a complete resolution of the large-scale structure of the turbulent flow, and the effect of the smaller scales, which are not acquired by this resolution, is modelled. Traditionally, the unresolved scales are distinguished from the resolved scales by the application of a spatial filter of limited extent. The computational effort required for LES may be less than the one for DNS, but it is still of substantial complexity. Hence, it is still not possible to perform LES for most of the turbulent flows arising in engineering applications. Nevertheless, it appears to be more auspicious to believe in LES than in DNS in the near future.

There is also a framework for dealing with multiscale problems of computational mechanics in general: the variational multiscale method. This theoretical framework was established by Hughes [2] and further developed as a powerful means for problems of computational mechanics having to deal with large ranges of scales by Hughes and co-workers [3, 4]. The basic concept consists in distinguishing scale groups, for example, large and small scales or resolved and unresolved scales, respectively. This methodical framework was also applied to the problem of the incompressible Navier–Stokes equations, in order to facilitate numerical simulations in the sense of LES. See Reference [5] for a theoretical elaboration and References [6, 7] for results of some early applications. In contrast to using a filter in traditional LES, variational projection separates scale ranges within the variational multiscale method. Aside from the use of a variational projection in preference to a spatial filter, the second characteristic feature of LES based on the variational multiscale method is that the direct influence of the subgrid-scale model is confined to the small resolved scales.

It should be remarked that the initial concept of the variational multiscale method as Hughes and co-workers proposed it in their publications assumes a separation of two scale ranges. Nevertheless, the framework allows various other arrangements going beyond this two-scale decomposition. Independently, Collis [8] and Gravemeier *et al.* [9] have recently broadened the variational multiscale method for LES by raising the number of separated scale ranges beyond the original twofold separation. A completely different numerical treatment for any of these ranges is enabled, for instance, by using the finite element method. The variational multiscale method is basically open for the application within a Galerkin finite element method, and this will, in fact, be the method of choice in this work. However, it is not restricted to this specific numerical method. At this stage, it should be pointed out that the variational multiscale method is, from a practical standpoint, 'merely' a theoretical framework for the separation of scales. Corresponding practical methods fitting in this framework, on the one hand, and enabling an implementation as a computational algorithm, on the other hand, are still rare. For such practical methods, it is crucial that a clear separation of the different ranges is actually achieved.

The Galerkin finite element method represents a hazardous choice for problems of fluid mechanics. Independent of the actual flow regime, it is, in general, not possible to achieve unspoilt results using the standard form of the Galerkin finite element method in case of a dominating convective term without resorting to an extremely fine discretization level. In Reference [10], it was proposed to apply a subgrid-scale model only to the small resolved scales, in order to preserve stability for a reasonably fine discretization. This approach is consistent with the second characteristic feature of LES based on the variational multiscale

 

method as mentioned above, although it was not applied in this specific context in Reference [10]. The second problem, which has to be dealt with in the context of the Navier–Stokes equations, is the required fulfillment of the so-called inf–sup condition, which is exhaustively described e.g. in Reference [11]. Recent work concerning the variational multiscale method within the finite element method can be found in References [12, 13].

In the present work, a practical implementation using a finite element method based on the separation of three scale ranges will be presented. This method is called 'three-level finite element method' (3LFEM). It has already been developed and applied to laminar flow situations in Reference [14]. The main features of this method are, on the one hand, its inherent stability without any demand for further measures with regard to the aforementioned numerical problems and, on the other hand, substantial computational savings on the small-scale level due to a localized approach. However, one has to 'pay' for this gain in computational efficiency by accepting a lower accuracy with respect to the smaller resolved scales, as will be seen below. In Section 2, a separation of two scales in the sense of a classical LES is brought into the framework of a Galerkin finite element method. Thus, the spatial filter in a classical LES is replaced by the variational projection of the Galerkin finite element method as the 'tool' for separating scale ranges. Section 3 contains the variational multiscale method in form of a three-scale separation. The combined strategy on the small-scale level based on residual-free bubbles and a stabilizing term is outlined in Section 3. The three-level finite element method presented in Section 4 represents the practical implementation following the theoretical considerations in the preceding sections. A comparative discussion with respect to the dynamic modelling procedure in Reference [15] and some remarks on the relative choice of the large- and small-scale spaces are the contents of Section 5. Two numerical examples are shown in Section 6. Finally, conclusions are drawn in Section 7.

## 2. LARGE EDDY SIMULATION WITHIN A GALERKIN FINITE ELEMENT METHOD

The set of incompressible Navier–Stokes equations is usually phrased in the primitive variables velocity $\mathbf{u}$ and kinematic pressure $p$, i.e. pressure divided by density. It is searched for $\mathbf{u}: \Omega \times (0,T) \to \mathbb{R}^d$ and $p: \Omega \times (0,T) \to \mathbb{R}$ such that

$$\frac{\partial \mathbf{u}}{\partial t} + \nabla \cdot (\mathbf{u} \otimes \mathbf{u}) + \nabla p - 2\nu \nabla \cdot \varepsilon(\mathbf{u}) = \mathbf{f} \quad \text{in } \Omega \times (0,T) \tag{1}$$

$$\nabla \cdot \mathbf{u} = 0 \quad \text{in } \Omega \times (0,T) \tag{2}$$

with the boundary conditions

$$\mathbf{u} = \mathbf{g} \quad \text{on } \Gamma_g \times (0,T) \tag{3}$$

$$\mathbf{n} \cdot \sigma = \mathbf{n} \cdot (-p\mathbf{I} + 2\nu\varepsilon(\mathbf{u})) = \mathbf{h} \quad \text{on } \Gamma_h \times (0,T) \tag{4}$$

and the initial condition

$$\mathbf{u} = \mathbf{u}_0 \quad \text{in } \Omega \times \{0\} \tag{5}$$

 

where the initial velocity field $\mathbf{u}_0$ is assumed to be divergence-free. The variational form of the Navier–Stokes equations is given as

$$B_{\mathrm{NS}}(\mathbf{v},q;\mathbf{u},p)=(\mathbf{v},\mathbf{f})_\Omega+(\mathbf{v},\mathbf{h})_{\Gamma_h} \tag{6}$$

where $\mathbf{v}$ and $q$ denote the weighting functions. The form $B_{\mathrm{NS}}(\mathbf{v},q;\mathbf{u},p)$ on the left-hand side of (6) is obtained after integrating by parts the viscous as well as the pressure term such that

$$B_{\mathrm{NS}}(\mathbf{v},q;\mathbf{u},p)=\left(\mathbf{v},\frac{\partial\mathbf{u}}{\partial t}\right)_\Omega+(\mathbf{v},\nabla\cdot(\mathbf{u}\otimes\mathbf{u}))_\Omega-(\nabla\cdot\mathbf{v},p)_\Omega+(\varepsilon(\mathbf{v}),2\nu\varepsilon(\mathbf{u}))_\Omega-(q,\nabla\cdot\mathbf{u})_\Omega \tag{7}$$

The $L_2$-inner product in the domain $\Omega$ or on the Neumann boundary $\Gamma_h$, respectively, on the right-hand side of (6) is defined as usual:

$$(\mathbf{v},\mathbf{f})_\Omega=\int_\Omega \mathbf{v}\mathbf{f}\,\mathrm{d}\Omega \tag{8}$$

The vectorial solution function space for the velocity is defined as

$$\mathscr{S}_{\mathbf{u}}=\{\mathbf{u}\in(H^1(\Omega))^d\,|\,\mathbf{u}=\mathbf{g}\ \text{on}\ \Gamma_g\} \tag{9}$$

and the corresponding weighting function space as

$$\mathscr{V}_{\mathbf{u}}=\{\mathbf{v}\in(H^1(\Omega))^d\,|\,\mathbf{v}=\mathbf{0}\ \text{on}\ \Gamma_g\} \tag{10}$$

The scalar solution function space for the pressure is given as

$$\mathscr{S}_p=L_{2,0}(\Omega)=\{p\in L_2(\Omega)\,|\,(p,1)_\Omega=0\} \tag{11}$$

if $\mathrm{meas}(\Gamma_h)=0$, else

$$\mathscr{S}_p=L_2(\Omega) \tag{12}$$

The corresponding weighting function space is defined as

$$\mathscr{V}_q=L_2(\Omega) \tag{13}$$

In combined form, the solution and weighting function spaces may be written as

$$\mathscr{S}_{\mathbf{u}p}:=\mathscr{S}_{\mathbf{u}}\times\mathscr{S}_p,\quad \mathscr{V}_{\mathbf{u}p}:=\mathscr{V}_{\mathbf{u}}\times\mathscr{V}_p \tag{14}$$

The interpretation of the Galerkin finite element method as a projection is extensively discussed in Reference [16, Appendix 3]. The main aspects for the underlying purpose are summarized in Reference [17]. Thus, this discussion may be omitted here, and the Galerkin projection will now be applied as an implicit filter for LES. For this purpose, an intuitive procedure will be followed here by adopting the separation of the velocity and the pressure from classical LES and incorporating them into the finite element framework as

$$\mathbf{u}=\mathbf{u}^h+\hat{\mathbf{u}},\quad p=p^h+\hat{p} \tag{15}$$

The resolved parts of the variables are indicated by the superscript $h$, which denotes the characteristic element length for scale resolution and, hence, specifies the size of the implicit

 

filter, and the unresolved terms by $\hat{(\cdot)}$. Decompositions (15) are then introduced into (6) yielding

$$B_{\mathrm{NS}}(\mathbf{v}^h, q^h; \mathbf{u}^h + \hat{\mathbf{u}}, p^h + \hat{p}) = (\mathbf{v}^h, \mathbf{f})_\Omega + (\mathbf{v}^h, \mathbf{h})_{\Gamma_h} \quad \forall \{\mathbf{v}^h, q^h\} \in \mathcal{V}^h_{\mathbf{u}p} \tag{16}$$

where $\mathcal{V}^h_{\mathbf{u}p}$ denotes the respective finite-dimensional weighting function space. The form $B_{\mathrm{NS}}$ is linearized according to Reference [5] by expanding it as

$$\begin{aligned} B_{\mathrm{NS}}(\mathbf{v}^h, q^h; \mathbf{u}^h + \hat{\mathbf{u}}, p^h + \hat{p}) &= B_{\mathrm{NS}}(\mathbf{v}^h, q^h; \mathbf{u}^h, p^h) + \frac{\mathrm{d}}{\mathrm{d}\varepsilon} B_{\mathrm{NS}}(\mathbf{v}^h, q^h; \mathbf{u}^h + \varepsilon\hat{\mathbf{u}}, p^h + \varepsilon\hat{p})|_{\varepsilon=0} \\ &\quad + \frac{\mathrm{d}^2}{\mathrm{d}\varepsilon^2} B_{\mathrm{NS}}(\mathbf{v}^h, q^h; \mathbf{u}^h + \varepsilon\hat{\mathbf{u}}, p^h + \varepsilon\hat{p})|_{\varepsilon=0} \\ &= B_{\mathrm{NS}}(\mathbf{v}^h, q^h; \mathbf{u}^h, p^h) + B^1_{\mathrm{NS}}(\mathbf{v}^h, q^h; \mathbf{u}^h, \hat{\mathbf{u}}, \hat{p}) + B^2_{\mathrm{NS}}(\mathbf{v}^h; \hat{\mathbf{u}}) \end{aligned} \tag{17}$$

where $B_{\mathrm{NS}}(\mathbf{v}^h, q^h; \mathbf{u}^h, p^h)$ is given according to (7),

$$\begin{aligned} B^1_{\mathrm{NS}}(\mathbf{v}^h, q^h; \mathbf{u}^h, \hat{\mathbf{u}}, \hat{p}) &= \frac{\mathrm{d}}{\mathrm{d}\varepsilon} B_{\mathrm{NS}}(\mathbf{v}^h, q^h; \mathbf{u}^h + \varepsilon\hat{\mathbf{u}}, p^h + \varepsilon\hat{p})|_{\varepsilon=0} \\ &= \left(\mathbf{v}^h, \frac{\partial\hat{\mathbf{u}}}{\partial t}\right)_\Omega + (\mathbf{v}^h, \nabla\cdot(\mathbf{u}^h \otimes \hat{\mathbf{u}}) + \nabla\cdot(\hat{\mathbf{u}} \otimes \mathbf{u}^h))_\Omega - (\nabla\cdot\mathbf{v}^h, \hat{p})_\Omega \\ &\quad + (\varepsilon(\mathbf{v}^h), 2\nu\varepsilon(\hat{\mathbf{u}}))_\Omega - (q^h, \nabla\cdot\hat{\mathbf{u}})_\Omega \end{aligned} \tag{18}$$

and

$$B^2_{\mathrm{NS}}(\mathbf{v}^h; \hat{\mathbf{u}}) = \frac{\mathrm{d}^2}{\mathrm{d}\varepsilon^2} B_{\mathrm{NS}}(\mathbf{v}^h, q^h; \mathbf{u}^h + \varepsilon\hat{\mathbf{u}}, p^h + \varepsilon\hat{p})|_{\varepsilon=0} = (\mathbf{v}^h, \nabla\cdot(\hat{\mathbf{u}} \otimes \hat{\mathbf{u}}))_\Omega \tag{19}$$

Rearranging (16) with the help of (17) yields

$$\begin{aligned} B_{\mathrm{NS}}(\mathbf{v}^h, q^h; \mathbf{u}^h, p^h) &= (\mathbf{v}^h, \mathbf{f})_\Omega + (\mathbf{v}^h, \mathbf{h})_{\Gamma_h} - B^1_{\mathrm{NS}}(\mathbf{v}^h, q^h; \mathbf{u}^h, \hat{\mathbf{u}}, \hat{p}) \\ &\quad - B^2_{\mathrm{NS}}(\mathbf{v}^h; \hat{\mathbf{u}}) \quad \forall \{\mathbf{v}^h, q^h\} \in \mathcal{V}^h_{\mathbf{u}p} \end{aligned} \tag{20}$$

The last two terms on the right-hand side of (20) may be identified as the influence of the unresolved scales onto the resolved scales. In terms of an interpretation of the Galerkin FEM as a projection, these two terms can be viewed as the projection of the unresolved scales onto the subspace of the resolved scales—and, hence, it is only this projection that has to be represented by a subgrid-scale model here, see also Reference [8].

It is accounted for the unknown projective terms on the right-hand side of (20) by a subgrid viscosity term according to the classical concept of Boussinesq. However, since it is intended to use equal-order element interpolations for velocity and pressure, a stabilization term in the sense of the PSPG-method according to Reference [18] is introduced additionally, in order to circumvent the inf–sup-condition which the standard Galerkin finite element formulation is subject to. The addition of these two terms to the left-hand side with the simultaneous omission of the two unknown (and, in fact, uncomputable) terms on the right-hand side

 

changes (20) to

$$B_{\mathrm{NS}}(\mathbf{v}^h, q^h; \mathbf{u}^h, p^h) + (\varepsilon(\mathbf{v}^h), 2\nu^{\mathrm{T}}\varepsilon(\mathbf{u}^h))_\Omega + \sum_{e=1}^{n_{\mathrm{el}}} (\nabla q^h, \tau_e^M \mathscr{R}_{\mathrm{NS}}^M(\mathbf{u}^h, p^h))_{\Omega_e}$$
$$= (\mathbf{v}^h, \mathbf{f})_\Omega + (\mathbf{v}^h, \mathbf{h})_{\Gamma_h} \quad \forall \{\mathbf{v}^h, q^h\} \in \mathscr{V}_{\mathbf{u}p}^h \tag{21}$$

where the subgrid viscosity is denoted by $\nu^{\mathrm{T}}$ and the residual of the Navier–Stokes momentum equation by $\mathscr{R}_{\mathrm{NS}}^M$. The stabilizing term is defined elementwise, i.e. for each element $e$ of the discretization with element domain $\Omega_e$, and summed over all $n_{\mathrm{el}}$ elements of the discretization. The algebraic stabilization parameter in the respective element is $\tau_e^M$. Appropriate formulas for the calculation of $\tau_e^M$ can be found in References [18, 19]. What remains to be specified is a modelling assumption for the subgrid viscosity $\nu^{\mathrm{T}}$. The Smagorinsky model [20] was the first subgrid-scale model and is still a commonly used one due to its attractive simplicity. It is given as

$$\nu^{\mathrm{T}} = (C_{\mathrm{S}} h)^2 |\varepsilon(\mathbf{u}^h)| \tag{22}$$

where the characteristic filter length $\Delta$ included in the original filter-based formulation is here replaced by the characteristic element length $h$ in LES based on a Galerkin projection. The weak point of the Smagorinsky model is represented by the constant $C_{\mathrm{S}}$ in (22). Numerous authors addressed this issue, and perhaps the most important improvement was achieved by the dynamic modelling procedure of Germano *et al.* [15], enabling a computation of $C_{\mathrm{S}}$ as a function of time and position. It is interesting to note that the dynamic modelling procedure already distinguishes large resolved scales, small resolved scales, and unresolved scales explicitly. This mirrors the type of scale separation to be presented in the following section.

## 3. VARIATIONAL MULTISCALE METHOD SEPARATING THREE SCALE RANGES

The main equation of the preceding section, (20), would have been obtained in similar form as the so-called 'large-scale equation', if a two-scale separation into large and small scales according to the original formulation of the variational multiscale method had been applied. In this case, the weighting functions in (20) would have been represented by their large-scale parts. Consequently, the corresponding small-scale equation would have revealed the same structure, with the small-scale parts of the weighting functions acting. Of course, there is no chance of actually solving this small-scale equation under the aforementioned circumstances. Thus, this equation may, in fact, be termed 'unresolved-scale equation' rather than small-scale equation, which precisely expresses this inability to solve it. Please consult Reference [17] for elaboration.

It is now intended to go one step further in separating three scale ranges. For this purpose, the solution and weighting function spaces are separated as follows:

$$\mathscr{S}_{\mathbf{u}p} = \bar{\mathscr{S}}_{\mathbf{u}p} \oplus \mathscr{S}'_{\mathbf{u}p} \oplus \hat{\mathscr{S}}_{\mathbf{u}p} \tag{23}$$

$$\mathscr{V}_{\mathbf{u}p} = \bar{\mathscr{V}}_{\mathbf{u}p} \oplus \mathscr{V}'_{\mathbf{u}p} \oplus \hat{\mathscr{V}}_{\mathbf{u}p} \tag{24}$$

In a discrete case, it is explicitly dealt with large resolved scales, which are indicated by $\overline{(\cdot)}$, small resolved scales, which are indicated by $(\cdot)'$, and unresolved scales. According to

 

this, the large- and small-scale function spaces are replaced by finite-dimensional spaces with characteristic element length $\bar{h}$ and $h'$, respectively, and the function space related to the unresolved scales of the problem is necessarily infinite-dimensional. For convenience of notation, the superscripts indicating the characteristic element lengths will be left out in the following. The equation system is given as

$$B_{\mathrm{NS}}(\bar{\mathbf{v}},\bar{q};\bar{\mathbf{u}}+\mathbf{u}'+\hat{\mathbf{u}},\bar{p}+p'+\hat{p})=(\bar{\mathbf{v}},\mathbf{f})_{\Omega}+(\bar{\mathbf{v}},\mathbf{h})_{\Gamma_h}\quad\forall\{\bar{\mathbf{v}},\bar{q}\}\in\mathscr{V}_{\bar{\mathbf{u}}p}^{\bar{h}} \tag{25}$$

$$B_{\mathrm{NS}}(\mathbf{v}',q';\bar{\mathbf{u}}+\mathbf{u}'+\hat{\mathbf{u}},\bar{p}+p'+\hat{p})=(\mathbf{v}',\mathbf{f})_{\Omega}+(\mathbf{v}',\mathbf{h})_{\Gamma_h}\quad\forall\{\mathbf{v}',q'\}\in\mathscr{V}_{\mathbf{u}p}^{h'} \tag{26}$$

$$B_{\mathrm{NS}}(\hat{\mathbf{v}},\hat{q};\bar{\mathbf{u}}+\mathbf{u}'+\hat{\mathbf{u}},\bar{p}+p'+\hat{p})=(\hat{\mathbf{v}},\mathbf{f})_{\Omega}+(\hat{\mathbf{v}},\mathbf{h})_{\Gamma_h}\quad\forall\{\hat{\mathbf{v}},\hat{q}\}\in\mathscr{V}_{\hat{\mathbf{u}}p}^{\hat{h}} \tag{27}$$

It is assumed that

$$B_{\mathrm{NS}}(\bar{\mathbf{v}},\bar{q};\hat{\mathbf{u}},\hat{p})\approx 0 \tag{28}$$

which relies on a clear separation of the large-scale space and the space of unresolved scales. As indicated in Reference [8], this amounts to be the first modelling step. Likewise the opposite projection is assumed to be

$$B_{\mathrm{NS}}(\hat{\mathbf{v}},\hat{q};\bar{\mathbf{u}},\bar{p})\approx 0 \tag{29}$$

These two assumptions lead to a simplified equation system by changing (25) to

$$B_{\mathrm{NS}}(\bar{\mathbf{v}},\bar{q};\bar{\mathbf{u}}+\mathbf{u}',\bar{p}+p')=(\bar{\mathbf{v}},\mathbf{f})_{\Omega}+(\bar{\mathbf{v}},\mathbf{h})_{\Gamma_h}\quad\forall\{\bar{\mathbf{v}},\bar{q}\}\in\mathscr{V}_{\bar{\mathbf{u}}p}^{\bar{h}} \tag{30}$$

and (27) to

$$B_{\mathrm{NS}}(\hat{\mathbf{v}},\hat{q};\mathbf{u}'+\hat{\mathbf{u}},p'+\hat{p})=(\hat{\mathbf{v}},\mathbf{f})_{\Omega}+(\hat{\mathbf{v}},\mathbf{h})_{\Gamma_h}\quad\forall\{\hat{\mathbf{v}},\hat{q}\}\in\mathscr{V}_{\hat{\mathbf{u}}p}^{\hat{h}} \tag{31}$$

whereas (26) remains unchanged.

It is not intended to resolve anything which is called 'unresolved' *a priori*. Taking into account the effect of the unresolved scales onto the small scales is the only desire. Several alternatives lend themselves to this purpose (see Reference [17]), but the focus here is on the subgrid viscosity approach. It should be emphasized that it is merely accounted for the dissipative effect of the unresolved scales onto the resolved scales by using this approach. The small-scale equation then reads

$$\begin{aligned}&B_{\mathrm{NS}}(\mathbf{v}',q';\bar{\mathbf{u}}+\mathbf{u}',\bar{p}+p')+(\varepsilon(\mathbf{v}'),2\nu'^{\mathrm{T}}\varepsilon(\mathbf{u}'))_{\Omega}\\&\quad=(\mathbf{v}',\mathbf{f})_{\Omega}+(\mathbf{v}',\mathbf{h})_{\Gamma_h}\quad\forall\{\mathbf{v}',q'\}\in\mathscr{V}_{\mathbf{u}p}^{h'}\end{aligned} \tag{32}$$

where the subgrid viscosity $\nu'^{\mathrm{T}}$ has to be distinguished from the subgrid viscosity $\nu^{\mathrm{T}}$ introduced in the previous section. It may be determined subject to a variety of model formulations, see Reference [17]. In the context of the dynamic modelling procedure to be presented below, however, it is not necessary to specify a particular model formulation like, for instance, the Smagorinsky model, since this dynamic modelling procedure aims at determining the value of the subgrid viscosity directly. Note that, due to assumption (28), the subgrid viscosity term

 

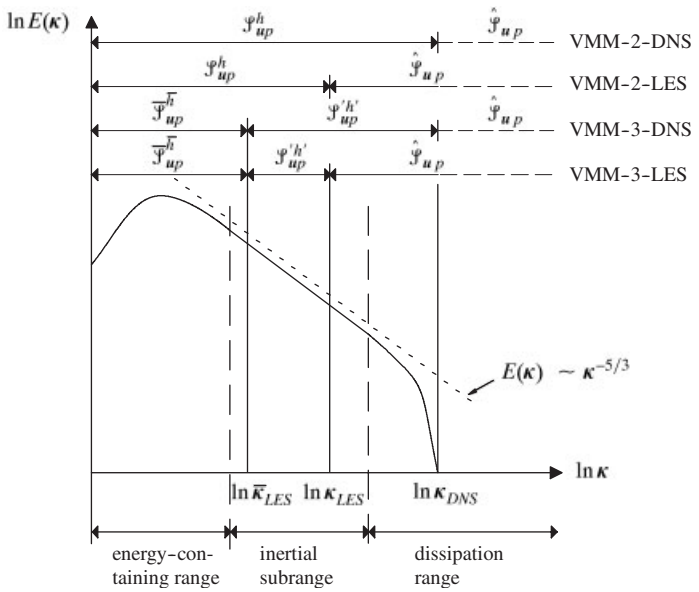


Figure 1. Kolmogorov energy spectrum for two- and three-scale separation of VMM.

directly acts only on the small resolved scales. Indirect influence on the large resolved scales, however, is ensured due to the coupling of the large- and the small-scale equations.

The three-scale separation represents a consequential extension of a two-scale separation, see References [14, 17]. In Figure 1, the Kolmogorov energy spectrum is displayed for the different situations of a two- and a three-scale separation. For clarity of notation, the superscripts indicating the characteristic element lengths are included in Figure 1. It is observable that there are two ways of performing DNS or LES. A DNS may result from completely resolving all scales necessary therefore by the large-scale space. Alternatively, the same may be done by distributing these scales among a large- and a small-scale space. Whereas this distinction may be more or less of academic nature for a DNS, it represents a crucial decision for a LES. In contrast to a two-scale LES, a three-scale LES provides one with the opportunity of letting the subgrid-scale model directly act only on the small-scale space, which is consistent with Equations (30)–(32). It has been dissected by Hughes and co-workers [5–7] that the crucial advantage of LES based on the variational multiscale method refers to the fact that the dissipative model directly acts only on the smaller of the resolved scales. Hence, the large scales are treated in a DNS-like manner, guaranteeing consistency, if adequate resolution is already achieved by the large-scale space. This last case represents a natural switch to a 'VMM-2-DNS', see Figure 1. It should be remarked that the idea of restricting the modelling efforts to the small scales may also be transferred back to the classical filter-based procedure. First ideas in this direction have recently been presented in Reference [21]. Finally, it is referred to Section 5, where this discussion will be renewed. In particular, a principal comparison to the dynamic modelling procedure of Germano *et al.* [15] will be carried out there, and some remarks concerning the choice of the absolute and relative size of the large- and small-scale space will be made.

 

## 3. COMBINED APPROACH FOR SMALL SCALES: RESIDUAL-FREE BUBBLES AND STABILIZING TERM

Using residual-free bubbles means obeying two basic rules:

- The governing differential equation has to be satisfied by the complete solution function in strong form on every individual element domain $\Omega_e$ of the basic discretization.
- Zero Dirichlet boundary conditions are assumed for the small-scale part of the solution function on the boundaries of every individual element domain $\Omega_e$.

For the underlying case of a separation of the resolved solution function into a large- and a small-scale part, following the above rules amounts to selecting the small-scale bubble part of the solution function such that the governing equation is solved in every individual element up to the large-scale part of the solution function. Correspondingly, the residual of the large-scale part of the solution function appears on the right-hand side of the residual-free bubble equation representing the 'driving force' of this equation. As aforementioned, this equation is subject to homogeneous Dirichlet boundary conditions. A selection of the respective literature addressing residual-free bubbles in general and, in particular, for convection–diffusion problems, authored by Brezzi, Farhat, Franca, Hughes, Russo and co-workers, is named: [22–26].

The strong form of the small-scale equation which corresponds to the weak form (32) reads

$$\frac{\partial \mathbf{u}'}{\partial t} + \nabla \cdot (\mathbf{u}' \otimes \mathbf{u}) + \nabla p' - 2(\nu + \nu_e'^{\mathrm{T}}) \nabla \cdot \varepsilon(\mathbf{u}')$$

$$= -\frac{\partial \bar{\mathbf{u}}}{\partial t} - \nabla \cdot (\bar{\mathbf{u}} \otimes \mathbf{u}) - \nabla \bar{p} + 2\nu \nabla \cdot \varepsilon(\bar{\mathbf{u}}) + \mathbf{f} \quad \text{in } \Omega_e \times (0, T) \tag{33}$$

$$\nabla \cdot \mathbf{u}' = -\nabla \cdot \bar{\mathbf{u}} \quad \text{in } \Omega_e \times (0, T) \tag{34}$$

$$\mathbf{u}' = \mathbf{0} \quad \text{on } \Gamma_e \times (0, T) \tag{35}$$

Note the zero Dirichlet boundary conditions on all element borders and the fact that $\nu_e'^{\mathrm{T}}$ is assumed to be constant within one element domain $\Omega_e$. The small-scale continuity equation (34) may be replaced by a small-scale pressure Poisson equation (PPE) as

$$\Delta p' + \nabla \cdot (\mathbf{u} \cdot \nabla \mathbf{u}' - \nu \Delta \mathbf{u}') = -\nabla \cdot [\mathscr{R}_{\mathrm{NS}}^{M}(\bar{\mathbf{u}}, \bar{p})] \quad \text{in } \Omega_e \times (0, T) \tag{36}$$

where the structure of a consistent PPE according to Reference [16] has been adapted for the small scales. The right-hand side of (36) is constituted by the negative divergence of the residual of the large-scale momentum equation.

Firstly, it is focussed on the small-scale momentum equation (33). To the authors' knowledge, the first attempt of using residual-free bubbles for the stabilization of a linearized stationary Navier–Stokes problem has to be credited to Russo [27]. The separation of function spaces, which is merely carried out for the weighting function space here, reads

$$\mathscr{V}_{\mathbf{u}p} \approx \mathscr{V}_{\mathbf{u}p}^{-} \oplus \mathscr{V}_{\mathbf{u},\mathrm{RFB}}' = \mathscr{V}_{\mathbf{u}p}^{-} \oplus_{\Omega_e} (B(\Omega_e))^d, \quad e = 1, \ldots, n_{\mathrm{el}} \tag{37}$$

 

with the usual assumption being $(B(\Omega_e))^d = (H_0^1(\Omega_e))^d$. As may be observed by inspecting the subscripts, the bubble space exclusively enhances the velocity approximation, i.e. $p' = 0$. Insights into approaches to satisfy the inf–sup condition emphasize the reasonability of this concept, see Reference [17]. By choosing $p' = 0$, a larger function space for the approximation of the velocity in comparison to the one for the approximation of the pressure is guaranteed. As a result, (33) can now be simplified to

$$\begin{aligned} &\frac{\partial \mathbf{u}'}{\partial t} + \nabla \cdot (\mathbf{u}' \otimes \mathbf{u}) - 2(\nu + \nu_e'^{\mathrm{T}}) \nabla \cdot \varepsilon(\mathbf{u}') \\ &\quad = -\frac{\partial \bar{\mathbf{u}}}{\partial t} - \nabla \cdot (\bar{\mathbf{u}} \otimes \mathbf{u}) - \nabla \bar{p} + 2\nu \nabla \cdot \varepsilon(\bar{\mathbf{u}}) + \mathbf{f} \quad \text{in } \Omega_e \times (0, T) \end{aligned} \tag{38}$$

If one were able to solve (38) in every element of the basic discretization, the small-scale velocity would be obtained as a sum of these elementwise solutions. The result for $\mathbf{u}'$, along with the assumption $p' = 0$, may then be integrated into the variational large-scale equation (30) leaving *one* final equation to be solved. Details of an approach which aims at solving directly for shape function components of the small-scale velocity as well as furthergoing assumptions, which enable such a separation into shape function components, are described in Reference [17]. The resulting shape function components of the small-scale velocity are eventually substituted into the large-scale equation in the course of a static condensation procedure.

Secondly, it is returned to the small-scale continuity equation (34) left out so far. Note that this equation is actually not needed any more, since there is no small-scale pressure in the small-scale momentum equation to be governed by the small-scale continuity equation. As will be seen below, however, it may be helpful to revitalize some kind of small-scale pressure, which is completely independent of the small-scale momentum equation. More precisely, it is focussed on the small-scale PPE (36) and tried to find a solution. This should be helpful in fulfilling the continuity condition on the small-scale level, an issue known to become more important with increasing Reynolds number, see e.g. References [16, 19, 28]. Therefore, it is supposed to be a crucial ingredient of the solution strategy, since this work deals with turbulent flows at relatively high Reynolds numbers.

The residual $\mathscr{R}_{\mathrm{NS}}^M(\bar{\mathbf{u}}, \bar{p})$ on the right-hand side of (36) is assumed to be divergence-free or else a potential component is subsumed in a modified small-scale pressure such that

$$\Delta p'_{\mathrm{mod}} = \Delta p' + \nabla \cdot [\mathscr{R}_{\mathrm{NS}}^M(\bar{\mathbf{u}}, \bar{p})] \tag{39}$$

The following Poisson equation for the modified small-scale pressure may be obtained from (36):

$$\Delta p'_{\mathrm{mod}} = -[\mathbf{u} \cdot \nabla(\nabla \cdot \bar{\mathbf{u}}) - \nu \Delta(\nabla \cdot \bar{\mathbf{u}})] = -[\mathbf{u} \cdot \nabla - \nu \Delta](\nabla \cdot \bar{\mathbf{u}}) \tag{40}$$

It is not advisable to solve this differential equation for the small-scale pressure on the element level besides the burden of solving the momentum equation, let alone the difficult question of useful pressure boundary conditions for (40) on the element boundaries. Here, it is rather intended to incorporate the effect of the small-scale pressure Poisson equation and, thus, the small-scale continuity equation into the final (large-scale) equation via an additional term in the form of a stabilizing term. Thus, $p'$ is approximated as

$$p' \approx -\tau_e^C (\nabla \cdot \bar{\mathbf{u}}) = -\tau_e^C \mathscr{R}_{\mathrm{NS}}^C(\bar{\mathbf{u}}) \tag{41}$$

 

where $\tau_e^C$ denotes an algebraic stabilization parameter and $\mathscr{R}_{\mathrm{NS}}^C(\bar{\mathbf{u}})$ the residual of the large-scale continuity equation. In the large-scale equation, a bulk viscosity term reading

$$\cdots + \sum_{e=1}^{n_{\mathrm{el}}} (\nabla \cdot \bar{\mathbf{v}}, \tau_e^C (\nabla \cdot \bar{\mathbf{u}}))_{\Omega_e} \cdots \tag{42}$$

is added to the left-hand side. Recently, it has been shown in Reference [29] that the derivation of this stabilizing term can be traced back to a potential introduction of something the authors call 'pressure bubble'. For $\tau_e^C$, the definition of Codina [30] is adopted as

$$\tau_e^C = \left[ v^2 + \left( \frac{c_2}{c_1} |\bar{\mathbf{u}}| h \right)^2 \right]^{1/2} \tag{43}$$

where the two constants are subject to

$$c_1 \geqslant c_2^2 \tag{44}$$

Finally, the strategy is summarized. Residual-free bubbles are used to solve the small-scale momentum equation. Additionally, the effect of the small-scale continuity equation is incorporated by taking it into account via a stabilizing term in the final (large-scale) equation. Thus, it is embarked on a combined residual-free bubble/stabilizing strategy. After all, the main assumption $p' = 0$ in the small-scale momentum equation means that the small-scale velocity is exclusively driven by the residual of the large-scale momentum equation and not by the residual of the continuity equation, see Reference [30]. Furthergoing discussions related to this assumption may be found in References [14, 17]. It should be emphasized that the strategy described in this section results in a completely stable method, i.e. there is no necessity to include any additional stabilizing term like, for instance, a PSPG-term as in the first line of (21).

## 4. THREE-LEVEL FINITE ELEMENT METHOD

The constituents of the three-level finite element method, i.e. the discretizations on the various levels and the solution strategy, are comprisingly depicted in Figure 2. Level 1 is represented by standard finite element spaces subject to (9)–(13) linked with a basic discretization. This basic discretization is the support of the large-scale part of the solution and also the 'source' of every further discretization on level 2 and 3, since these discretizations are restricted to individual elements of the basic discretization. Level 2 and 3 will be detailed in the following. The stabilizing term in the form of a bulk viscosity term (BVT), which is eventually added to the final (large-scale) equation besides the approximate residual-free bubble (RFB) functions, is also indicated in Figure 2.

### *4.1. Level 2: approximate residual-free bubble functions based on elementwise submeshes*

The idea of using a two-level finite element method for the practical computation of residual-free bubble functions can be traced back to Reference [31], where this methodology was proposed for the Helmholtz equation. In the same year, the application of this approach to convection–diffusion equations was published in Reference [32]. Afterwards, Nesliturk and Franca also dealt with the stationary incompressible Navier–Stokes equations [33, 34]. In

 

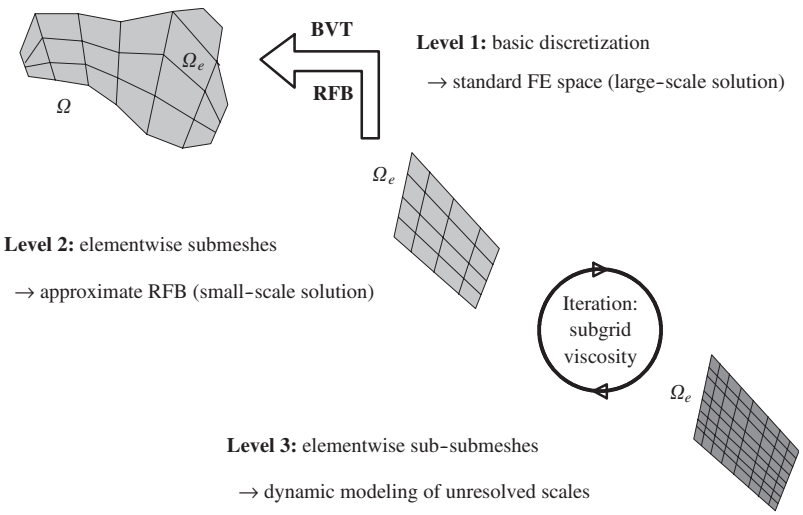


Figure 2. Three-level finite element method: discretizations and strategy.

Reference [14], the basic idea of this method was extended in order to use it for the instationary incompressible Navier–Stokes equations being semi-discretized in time. At the same time, the validity of this approach for any kind of convection–diffusion-reaction equation was shown.

On every individual element domain $\Omega_e$, a submesh is introduced. This discretization on a second level or, more precisely, the number of $n_{\mathrm{el}}$ discretizations on a second level is the support for the small-scale part of the solution, i.e. the small-scale momentum equation (38) subject to the residual-free bubble assumption. As aforementioned, (38) may be decomposed into its basic shape function components. The decomposition process is described in detail in Reference [17]. Finally, one obtains a certain number of scalar convection–diffusion-reaction equations with identical left-hand side structure and varying right-hand sides. Due to this, a representative equation in the form of a normalized equation, i.e. an equation with the right-hand side equal to one, is used below to explain the solution process on the second and third level. This normalized residual-free bubble equation is given as

$$\mathbf{u}\cdot\nabla\mathscr{B}_1 - \nu\Delta\mathscr{B}_1 + \frac{1}{\delta t}\mathscr{B}_1 = 1 \quad \text{in } \Omega_e \tag{45}$$

subject to the usual zero Dirichlet boundary conditions. In (45), $\mathscr{B}_1$ represents a place-holder for the respective shape function components. In order to obtain (45) starting from (38), both the convective and the viscous term have been simplified using the continuity condition, and the subgrid viscosity has been omitted for the time being.

Since one is normally unable to find an analytical solution to even this simplified equation (45), it is attempted to find an approximate residual-free bubble function $\mathscr{B}_1^{\mathrm{SM}}$ in every element of the original discretization. This is done with the aid of the elementwise submeshes (SM). The approximate residual-free bubble $\mathscr{B}_1^{\mathrm{SM}}$ then replaces the actually sought-after exact residual-free bubble function $\mathscr{B}_1$. The variational form of (45) with the submesh weighting

 

functions $w^{\mathrm{SM}}$ is given as

$$\left(w^{\mathrm{SM}}, \mathbf{u}\cdot\nabla\mathscr{B}_1^{\mathrm{SM}} + \frac{1}{\delta t}\,\mathscr{B}_1^{\mathrm{SM}}\right)_{\Omega_e} + (\nabla w^{\mathrm{SM}}, \nu\nabla\mathscr{B}_1^{\mathrm{SM}})_{\Omega_e} = (w^{\mathrm{SM}}, 1)_{\Omega_e} \tag{46}$$

*4.2. Level 3: dynamic modelling of unresolved scales based on elementwise sub-submeshes*

If one were able to solve the variational problem (46), at least up to the necessary resolution limit for a complete incorporation of all existing scales in the sense of a DNS, a fully satisfying local solution for the small scales within every individual element domain $\Omega_e$ would be achieved. Of course, this solution is limited from a global perspective by the aforementioned assumptions, in particular the crucial residual-free bubble assumption that the scales crossing the element boundaries are not taken into account. As attractive this thought may still be, as unlikely is it, in general, due to limited computer power. However, obtaining at least a good approximation of $\mathscr{B}_1$ would be the second best choice and, more importantly, the one which can be afforded in general. The idea for this is basically the same as the idea underlying the subgrid viscosity concept in a global context. Here, the elementwise equations are likewise enhanced by the addition of a subgrid viscosity term. Thus, the quality of the approximation as a whole depends on the quality of the approximation of the elementwise subgrid viscosity $\nu_e'^{\mathrm{T}}$. The enhanced variational problem is given as

$$\left(w^{\mathrm{SM}}, \mathbf{u}\cdot\nabla\mathscr{B}_1^{\mathrm{SM}} + \frac{1}{\delta t}\,\mathscr{B}_1^{\mathrm{SM}}\right)_{\Omega_e} + (\nabla w^{\mathrm{SM}}, (\nu + \nu_e'^{\mathrm{T}})\nabla\mathscr{B}_1^{\mathrm{SM}})_{\Omega_e} = (w^{\mathrm{SM}}, 1)_{\Omega_e} \tag{47}$$

In order to reach beyond the limitations of a model based on an unknown constant like the Smagorinsky model (22), a dynamic modelling procedure is chosen here. In Reference [35], a dynamic tune-up for $\nu_e'^{\mathrm{T}}$ was proposed from which a reasonably good value should arise. Brezzi *et al.* [35] assumed a model formulation previously suggested in Reference [10] to be the basis of their dynamic algorithm, which exhibits an obvious similarity with (22). In Reference [17], it was shown that there was actually no need for any model assumption, since a direct calculation of the subgrid viscosity is possible.

For the dynamic modelling procedure, a sub-submesh (SSM) is chosen, which is slightly finer than the original submesh (SM) and on which the variational equation (47) has to be solved as well. Comparing these two solutions, the desired 'good' value for $\nu_e'^{\mathrm{T}}$ may be achieved. However, for this dynamic tune-up to be workable, in that an explicit value can be obtained in the end, a criterion has to be established. Motivated by insights from the theory of stabilized methods, the average integral of $\mathscr{B}_1$ on the large-scale element domain $\Omega_e$ is required to be equal to the corresponding value of the adequately resolved bubble for $\nu_e'^{\mathrm{T}} = 0$ in (47) such that

$$\frac{1}{|\Omega_e|}\int_{\Omega_e}\mathscr{B}_1(\nu_e'^{\mathrm{T}} = 0)\,\mathrm{d}\Omega_e \approx \frac{1}{|\Omega_e|}\int_{\Omega_e}\mathscr{B}_1^{\mathrm{SM}}(\nu_e'^{\mathrm{T}})\,\mathrm{d}\Omega_e \approx \frac{1}{|\Omega_e|}\int_{\Omega_e}\mathscr{B}_1^{\mathrm{SSM}}(\nu_e'^{\mathrm{T}})\,\mathrm{d}\Omega_e \tag{48}$$

where the solution on the sub-submesh is indicated by the superscript SSM, see Reference [35]. Criterion (48) governs an iterative algorithm amounting to be an extrapolation, with the target of this extrapolation (hopefully) being the goal: a 'good' approximation of the analytical residual-free bubble $\mathscr{B}_1$, i.e. the one for $\nu_e'^{\mathrm{T}} = 0$. Variations of criterion (48) potentially better suited for turbulent flow applications are certainly conceivable, and it is intended

 

to pursue them in future. The details of the dynamic modelling procedure can be found in References [14, 17].

## 5. DISCUSSION

In Figure 3, a principal comparison is drawn between the dynamic modelling procedure of Germano *et al.* [15] and the 'VMM-3-LES' with the dynamic modelling procedure outlined above. Besides the fact that the subgrid-scale model acts on the complete range of resolved scales in classical LES, which is definitely not a specific feature of the dynamic modelling procedure of Germano *et al.* [15], the crucial difference pointed out in Figure 3 refers to the range of scales exploited to fix the undetermined constant in the respective model. In the dynamic modelling procedure of Germano *et al.* [15], the small resolved scales are exploited, and the constant is calculated based on the Germano identity. In the 'VMM-3-LES' with the respective dynamic modelling procedure, the unresolved scales are, so far in a crude manner (see Reference [17] for discussion), estimated, and the resulting model is then applied to the small resolved scales. Furthermore, the approximation of the small resolved scales via the localized residual-free bubble strategy should be reemphasized.

The underlying idea and the reason for the success of the dynamic modelling procedure in Germano *et al.* [15] has to be found in the hypothesis of the similarity between the unresolved scales and the small resolved scales. It is, however, certainly unquestionable that no scales are more similar to the unresolved scales than the unresolved scales themselves. Thus, a dynamic modelling procedure estimating the unresolved scales appears to be promising in the authors' point of view, although the actual estimation is still crude.

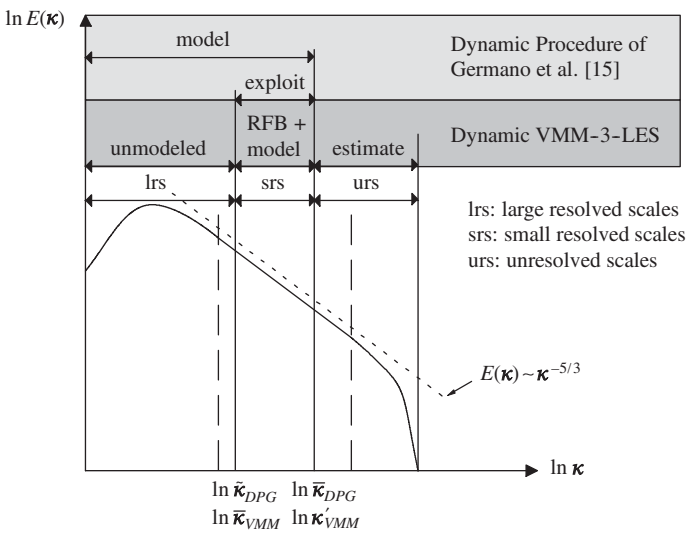


Figure 3. Comparing the dynamic procedure of Germano *et al.* [15] to the dynamic VMM-3-LES.

 

A final remark in this context is devoted to the important question of how large the size of the space containing the large as well as the small resolved scales should be chosen both absolutely and in comparison to each other. In general, it should be remarked that using a variational projection allows for a clear separation of scales and, accordingly, scale spaces in contrast to, for example, discrete smooth filters, which are widely used in traditional LES. The combined extension of both spaces is definitely restricted by the computational effort which can be afforded overall. This essential restriction for the overall size of both spaces, however, still leaves room for deciding on the relative extension of the spaces. A first basic requirement for choosing the 'cutoff-level' of the large-scale space may demand this space to cover at least the range of energy-containing modes, i.e. alternatively expressed, the location of the 'cutoff-level' is supposed to be within the inertial subrange. This basic requirement has already been taken into account in the depiction of the Kolmogorov energy spectrum in Figure 1. Aside from this, several numerical tests of the dynamic modelling procedure according to Germano *et al.* [15] revealed an optimal value for the 'cutoff-level' associated with a test filter $\widetilde{(\cdot)}$ which is about twice as large as the one associated with the basic filter $\overline{(\cdot)}$, see e.g. Reference [1]. This may also be accepted as a first hint for an adequate choice of the respective relation of large- and small-scale space within the variational multiscale method. It is also referred to the related discussion in Reference [5].

It is without doubt that the aforementioned choices strongly affect the actual impact of a potential subgrid-scale model. On the one hand, the combined size of large- and small-scale space influences the overall impact. For a very fine resolution, i.e. a very large size of large- and small-scale space together, there are only few unresolved scales left to be modelled. However, the overall impact of the subgrid-scale model will become crucial, if this combined resolution of large- and small-scale space is rather poor. This rather general perception is definitely valid for both ways of performing LES, the traditional and the multiscale approach. On the other hand, the relative size of large- and small-scale space influences the specific impact within the variational multiscale method. A dominant large-scale space in comparison to the small-scale space leaves the majority of the scales without the addition of a modelling term. This eventually results in a pure DNS for the extreme case that all scales, with no unresolved scales left, are actually contained in the large-scale space. In contrast to this, a diminutive large-scale space tends towards the classical approach of LES again, since the subgrid-scale model is added to a substantial margin of the resolved scales. Here, the extreme case with all scales, but still leaving unresolved scales, contained in the small-scale space has to be considered as the classical LES approach again. It should be remarked that this last case is not feasible using residual-free bubbles for approximating the small-scale part of the solution. For further discussion, it is referred to Reference [8].

Concluding this discussion, it may simply be reiterated that the absolute as well as the relative choice of the respective spaces considerably influences the overall procedure. In fact, its actual selection is an important parameter of the method. Aside from this, it is undoubted that the scope of the particular method based on residual-free bubbles is explicitly limited. The restriction of the small-scale solutions to individual element domains of the basic discretization basically appears to demand a dominant large-scale space in return. Nevertheless, the numerical simulations of turbulent flow situations to be described in the following section are conducted with rather coarse large-scale spaces, in order to gain an impression about the performance of this particular method under these less favourable, yet rather affordable, circumstances.

 

## 6. NUMERICAL EXAMPLES

### *6.1. Lid-driven cavity flow (3-D)*

The turbulent recirculating flow in a 3-D lid-driven cavity exhibits the occurrence of Taylor–Görtler-type vortices, which are formed as a result of the curvature of the streamlines due to the first vortex. Experimental data are reported in Reference [36] for flows at Reynolds numbers 3200, 5000, 7500, and 10 000 inside cavities with varying spanwise aspect ratio (SAR). The SAR is defined as the ratio of the lengths of the cavity in $x_3$ and in $x_1$ direction. Zang *et al.* [37] performed LES using a finite volume method with the dynamic modelling procedure of Germano *et al.* [15], which they called DSM, and a dynamic mixed model (DMM), where they, additionally, took into account the scale similarity model according to Bardina *et al.* [38]. Three cases are reported in Reference [37]: a flow at Reynolds number 3200 and SAR of the cavity being 1.0 on a $32 \times 32 \times 32$ grid as well as flows at Reynolds numbers 7500 and 10 000, respectively, with SAR of the cavity being 0.5 on a $64 \times 64 \times 32$ grid. The grid points are clustered near the walls in $x_1$ and $x_2$ direction, with the smallest control volume length in these directions being 0.01 for Reynolds numbers 3200 and 7500 as well as 0.005 for Reynolds number 10 000, respectively. Based on the experimental data in Reference [36], they describe the flow at Reynolds number 3200 to be essentially laminar, although an inherent unsteadiness may occur. At Reynolds number 7500, a transitional stage is reached, since the flow becomes unstable near the downstream eddy for Reynolds numbers higher than about 6000. At even higher Reynolds number of about 10 000, the flow becomes fully turbulent. Thus, laminar, transitional, and turbulent regimes were covered by choosing these three cases in Reference [37]. Further numerical studies using a finite element method can be found in References [39, 40].

Following the guidelines of Reference [37], the three Reynolds numbers 3200, 7500, and 10 000 are studied here as well. However, all three flows are considered in a cavity with SAR 1.0, i.e. a cavity with unit length in all three coordinate directions. No-slip boundary conditions for the velocity are assumed on all cavity walls, except the top wall, where a velocity of 1.0 in $x_1$ direction is prescribed. The pressure is prescribed at one node of the bottom wall, in order to fix the constant the pressure is determined up to in a problem with Dirichlet boundary conditions at all boundaries. A relatively coarse basic discretization with $16 \times 16 \times 16$ trilinear hexahedral elements is chosen for all flow situations. This corresponds to 10 125 velocity and 3374 pressure degrees of freedom, respectively, related to the basic discretization. The discretization is linearly refined towards the walls in $x_1$ and $x_2$ direction with the smallest element length being 0.02 in these directions. For the second level of the two-level method, uniform elementwise submeshes with $4 \times 4 \times 4$ elements are chosen. For the second and third level of the three-level method, uniform elementwise submeshes with $3 \times 3 \times 3$ elements and sub-submeshes with $4 \times 4 \times 4$ elements are chosen, respectively. This overall choice of coarse discretizations on all three levels is consistent with the predominant goal of investigating the performance of the considered methods with a relatively coarse resolution.

Analog to what is done in References [37, 40], an impulsive start is performed, i.e. the initial condition is a zero velocity field. The Crank–Nicolson scheme is used for the temporal discretization with a time step $\delta t = 0.1$ time units. A time scale $T_{\text{cav}}$ is defined in Reference [37] to be the estimated time for a particle at the edge of the top boundary layer to travel

 

back to its starting position. This time scale is roughly estimated to be about 10 time units for the present simulations. Initially, each simulation is run for five time scales $T_{\text{cav}}$, i.e. 50 time units or 500 time steps. Within this time period, the flow is expected to develop to full extent including a subsequent relaxation time. Afterwards, statistics are collected for another five time scales $T_{\text{cav}}$.

All results are compared to the experimental data of Reference [36]. Unfortunately, the experimental data for the flow at Reynolds number 7500 was only evaluated for one half of the cavity. Moreover, the numerical simulations in Reference [37] were merely performed for a cavity with SAR 0.5 at Reynolds numbers 7500 and 10 000. Thus, a direct comparison with these numerical data is not feasible. The mean velocities $\langle u_1 \rangle$ and $\langle u_2 \rangle$, which are evaluated as a discrete time average, are analysed on the centrelines $x_1 = 0.5$ and $x_2 = 0.5$, respectively, in the mid-plane of the cavity, i.e. in the plane $x_3 = 0.5$. Furthermore, the root-mean-square values of the velocities $u_1$ and $u_2$ as well as the component $\langle u_1^f u_2^f \rangle$ of the Reynolds stress tensor are evaluated, where $u_i^f$ denotes the fluctuating velocity component in $x_i$ direction. The root-mean-square values and the Reynolds stress components are multiplied by the amplification factors 10 and 500, respectively, in order to guarantee a reasonable visual impression of these values within the respective diagrams. Additionally, the temporal evolution of the total kinetic energy in the domain $\Omega$ of the cavity subject to

$$E_{\text{kin}}(\mathbf{u}^h) = \frac{1}{2} \int_\Omega \mathbf{u}^h \cdot \mathbf{u}^h \, \mathrm{d}\Omega \tag{49}$$

is depicted.

Various methods are investigated. Firstly, a stabilized method of USFEM-type (see e.g. Reference [41]) is applied. Secondly, the Smagorinsky model is employed in a PSPG finite element method according to (21). The Smagorinsky constant is fixed to be $C_{\text{S}} = 0.1$, and the element length $\bar{h}$ is defined to be the cubic root of the element volume, i.e. $\bar{h} = \frac{1}{16}$ for the present discretization. Thirdly, the two-level method and the three-level method with dynamic as well as 'static' modelling are used. At Reynolds numbers 3200 and 7500, results obtained with the dynamic modelling procedure are reported. At Reynolds number 10 000, results obtained by applying the Smagorinsky model with $C_{\text{S}} = 0.1$ as a 'static' way of modelling are reported. This last case may clearly exhibit differences between the application of the relatively simple and, hence, computationally efficient Smagorinsky model on level 2 and the application one level 'lower' on level 3. Further results obtained using dynamic and 'static' models within the multi-level methods for flows at other Reynolds numbers, which are not reported here, have not revealed distinctive features in significant contrast to the ones given here.

Figures 4–6 display the temporal evolution of the total kinetic energy for the three investigated cases. The introduction of various amounts of numerical viscosity bears an interesting consequence for the results of this flow example. It is well-known from the physical point of view that the higher the physical viscosity of the flow, the larger is the zone of influence of the prescribed velocity at the top boundary of cavity. Simply spoken, the higher the physical viscosity, the larger are the extensions of the layers at the respective boundaries of the cavity towards the centre of the cavity. Here, this leads to the fact that the method which is supposed to introduce the highest amount of numerical viscosity also exhibits the highest values of the total kinetic energy throughout the simulation. This is observed at all three Reynolds numbers.

 

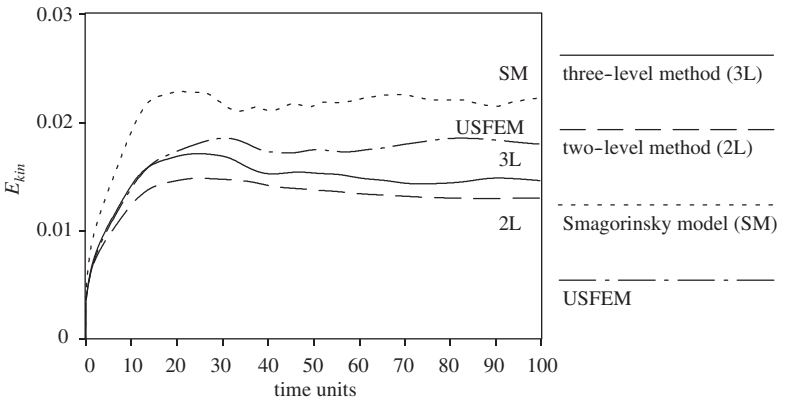


Figure 4. Temporal evolution of total kinetic energy at $Re = 3200$.

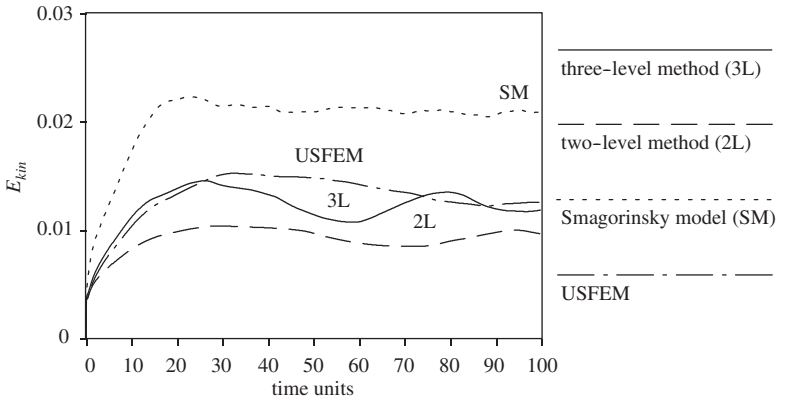


Figure 5. Temporal evolution of total kinetic energy at $Re = 7500$.

The three-level method and the USFEM bear about the same amount of numerical viscosity at Reynolds numbers 7500 and 10 000, see Figures 5 and 6. The USFEM is more viscous at the lowest Reynolds number 3200, see Figure 4. The two-level method introduces the least numerical viscosity in every considered case. This discrepancy becomes quite substantial at higher Reynolds numbers.

As expected, sample calculations using higher and lower values for the Smagorinsky constant have yielded respective higher and lower values of the total kinetic energy. Furthermore, a test calculation with an alternative definition of the characteristic element length $\bar{h}$, namely the streamlength, i.e. the length of the element in streamline direction, has led to a substantially higher value of the total kinetic energy. This result for such an element length definition, which is often used for the stability parameter calculation within stabilized methods, has to be expected, since it usually produces a larger element length $\bar{h}$ than the one obtained as the cubic root of the element volume. This emphasizes the sensitivity of the results to the

 

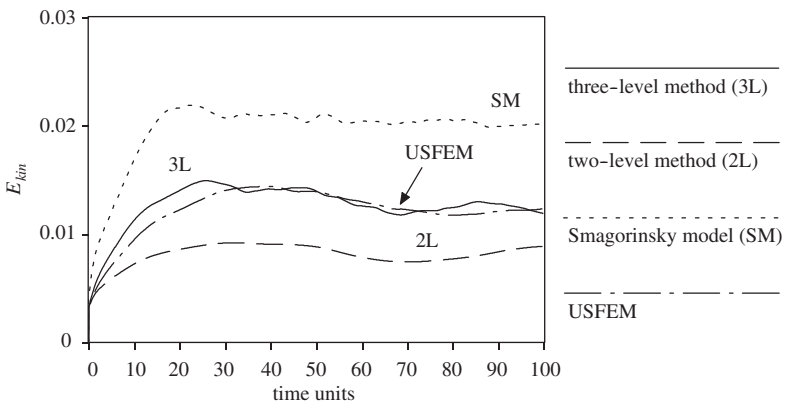


Figure 6. Temporal evolution of total kinetic energy at $Re = 10\,000$.

choice of the Smagorinsky constant as well as the element length definition. This was also investigated in Reference [37], where the authors display the progression of the Smagorinsky constant obtained via the dynamic procedures DSM and DMM throughout the centrelines in the mid-plane. They were able to show that $C_S$ from DMM is nearly everywhere, except from a few peaks, substantially smaller than 0.1. In comparison, DSM produces considerably larger values.

The profiles for the mean velocities $\langle u_1 \rangle$ and $\langle u_2 \rangle$ on the centrelines in the mid-plane of the cavity for the various cases are analysed in Figures 7(a), 8(a), and 9(a). It is stated that the USFEM as well as, in particular, the PSPG method with the Smagorinsky model overpredict the experimentally determined velocity values and the two- as well as three-level method underestimate them at Reynolds number 3200, with one noticeable exception for $\langle u_2 \rangle$ at the right boundary. At Reynolds numbers 7500 and 10 000, the two- and, in particular, the three-level method exhibit a remarkably good agreement with the experimental data, even with the present coarse basic discretization. The Smagorinsky model as well as the USFEM still overpredict at these Reynolds numbers.

This good prediction is not maintained for the root-mean-square values and, in particular, the components of the Reynolds stress. The general tendency of the experimental curve for the root-mean-square values at Reynolds number 3200 in Figure 7(b) is reproduced by the various methods. The Smagorinsky model is the only method which, on the one hand, correctly predicts the lower peak of the vertical curve and, on the other hand, overpredicts both peaks of the horizontal curve. Similar observations, however in a more distinct manner, are made for the Reynolds stresses depicted in Figure 7(c). It should be emphasized that mispredictions of various peaks of these curves, although less articulate, can also be found in the numerical results of Reference [37], which were achieved with a two times finer discretization in each coordinate direction. Some noticeable deviations may even be observed in the numerical results of Reference [39], which were obtained using an almost four times finer discretization in each coordinate direction. These observations underline the difficulty in predicting these values. Aside from this, experimental uncertainties cannot be ruled out completely either. Under these circumstances, it is stated that the root-mean-square values in Figures 8(b) and 9(b), at least partly, as well as the Reynolds stresses in Figures 8(c) and 9(c) for the most part,

 

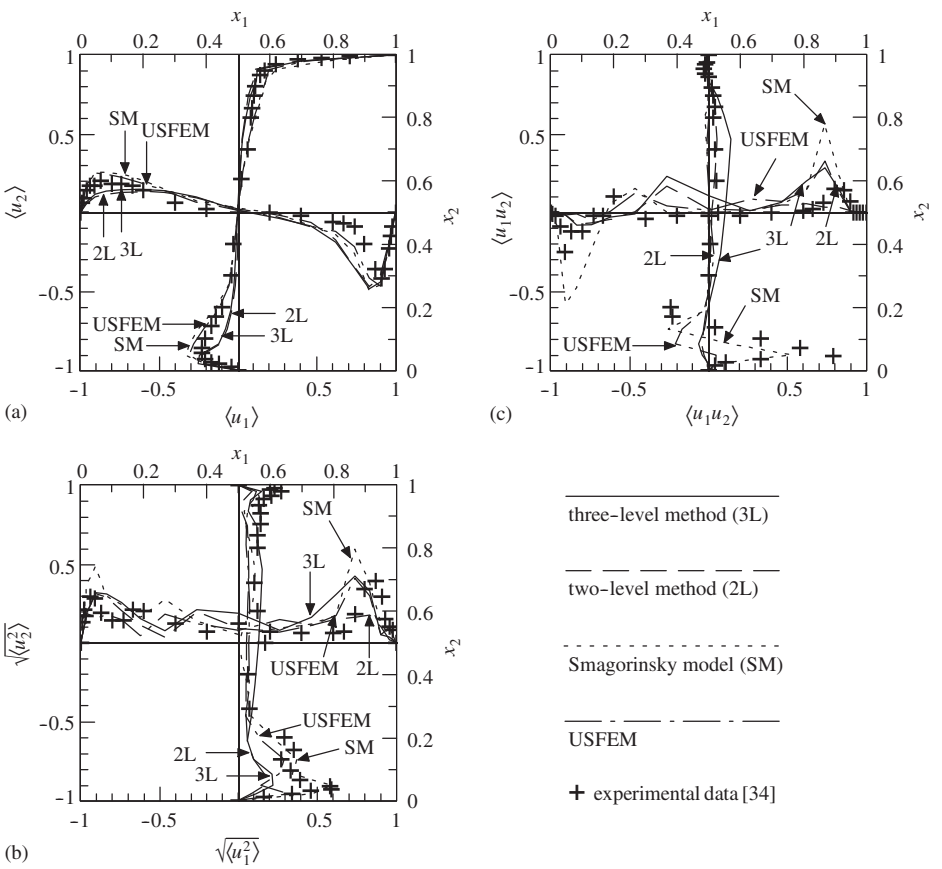


Figure 7. Variables on the centrelines in the mid-plane for $Re = 3200$ and SAR 1.0: (a) mean velocities; (b) rms velocities (factor 10); and (c) Reynolds stress (factor 500).

respectively, cannot be considered as a sufficient prediction of the experimental data for all applied methods. Most probably, the relatively coarse basic discretization, which has been chosen for the present simulations, simply has to be considered as being insufficient, at least for a correct predicition of these extremely sensitive values.

### *6.2. Plane mixing layer (2-D)*

Mixing layers are encountered in aerodynamics, in the atmosphere or the ocean, e.g. in the wake of mountains, in the Gulf stream or in the Mediterranean sea, as well as in the atmospheres of Jupiter and Saturn at the interface between neighbouring zonal jets, see e.g. Reference [42]. It is actually a flow developing far away from boundaries, and, thus, the influence of boundaries is eliminated in this flow example. As an answer to potential objections that a two-dimensional flow does not lead to what is usually perceived as 'turbulence', the following features of the flow considering it to be 'turbulent in a certain sense' may be

 

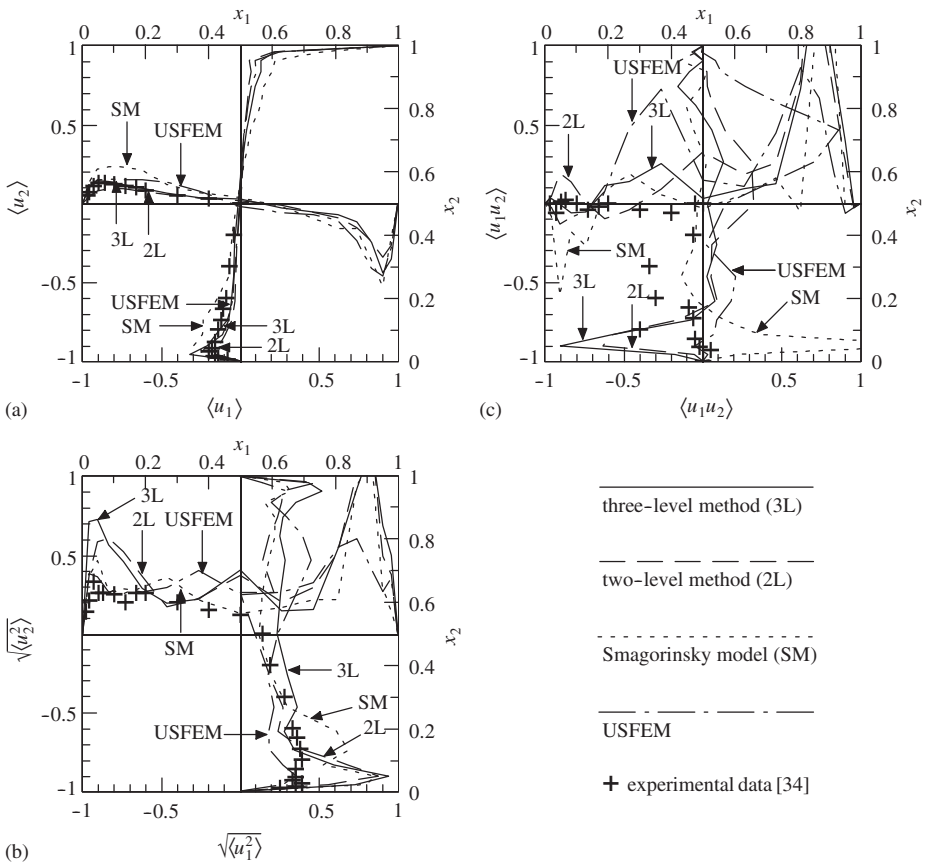


Figure 8. Variables on the centrelines in the mid-plane for $Re = 7500$ and SAR 1.0: (a) mean velocities; (b) rms velocities (factor 10); and (c) Reynolds stress (factor 500).

returned according to Reference [42]:

- The flow is extremely sensitive to the initial condition. In fact, it would be completely unpredictable in an infinite domain. This was proven by investigating two flows which were initially very close in the relevant parameters. In an infinite domain, these two flows would show a complete decorrelation. Only the finite domain, which has to be chosen for the simulation being viable, 'prevents' the flow from being completely unpredictable.
- After a first pairing, which will be described below, a broadband energy spectrum of slope intermediate between $k^{-4}$ and $k^{-3}$ is developed. The interaction between two- and three-dimensional turbulence related to this flow situation was elaborated in Reference [42, Section 4].

Aside from this important physical rationale for choosing this flow example as a 'turbulent' flow example, a much more pragmatic point of view qualifies a 2-D flow example as a legitimate test case for the present methods by saying that, if the methods do not work properly for a 2-D example, it will be unlikely to work for any 3-D example.

 

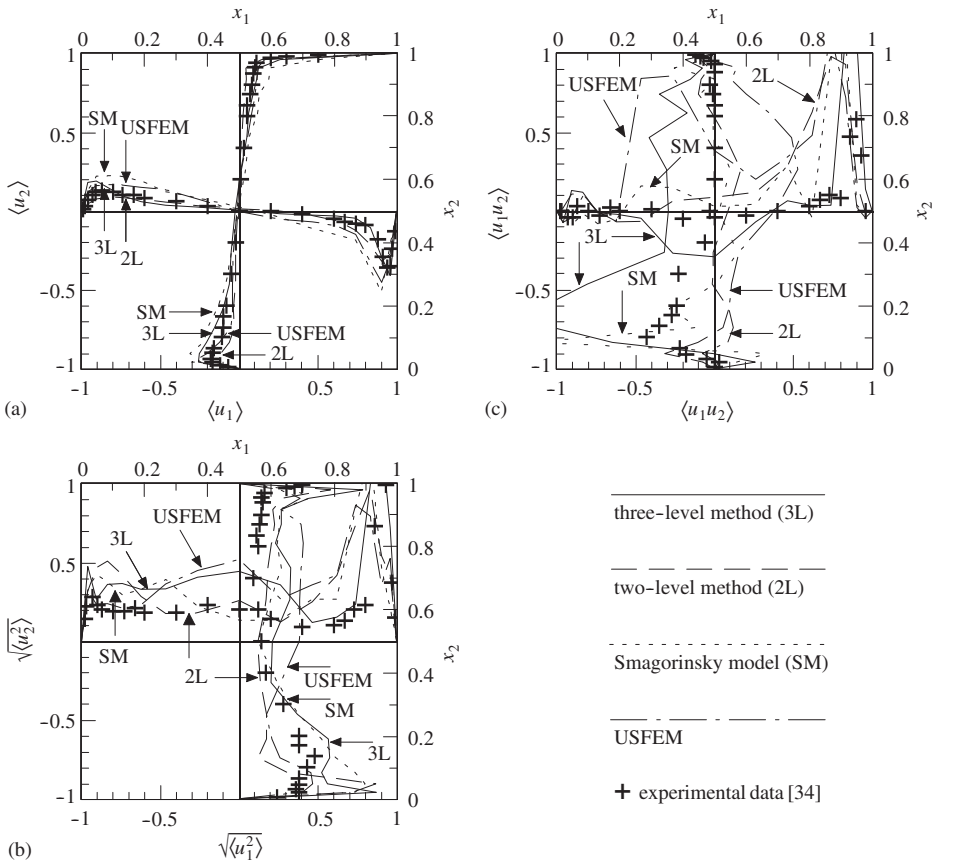


Figure 9. Variables on the centrelines in the mid-plane for $Re = 10\,000$ and SAR 1.0: (a) mean velocities; (b) rms velocities (factor 10); and (c) Reynolds stress (factor 500).

The domain of the problem is defined to be $\Omega = [0, 1] \times [0, 1]$, see Figure 10(a). No, i.e. free-slip, boundary conditions are applied at the boundaries $x_2 = 0$ as well as $x_2 = 1$ and periodic boundary conditions at the boundaries $x_1 = 0$ as well as $x_1 = 1$. The pressure is prescribed to be zero at the mid-point $x_1 = 0.5$ of the lower boundary $x_2 = 0$. The initial velocity field is given by a hyperbolic tangent profile as

$$u_1(x_2) = u_{1,\max} \tanh\left(\frac{2x_2 - 1}{\delta_0}\right) \tag{50}$$

where $\delta_0$ denotes the initial vorticity thickness. According to Reference [43], $\delta_0$ is chosen to be $\frac{1}{28}$. The velocity component $u_2$ is assumed to be zero initially. The initial velocity distribution (50) is displayed in Figure 10(b).

 

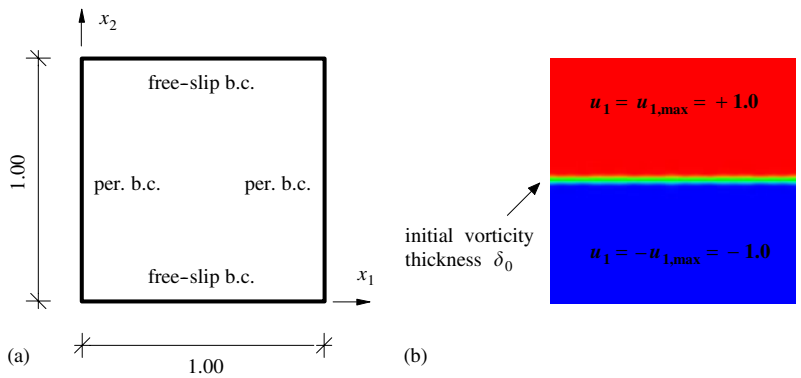


Figure 10. Plane mixing layer: (a) domain with boundary conditions; and (b) coloured initial velocity distribution.

A white-noise perturbation of small amplitude is imposed on the initial velocity field, expressed in a streamfunction formulation as

$$\psi_{\text{per}} = c_{\text{noise}} u_{1,\max}\, \mathrm{e}^{-((x_2-0.5)/\delta_0)^2}\, \cos(\alpha x_1) \tag{51}$$

It may be proven by the reader that this perturbation is divergence-free. The corresponding wavenumber is $\alpha = 2\pi/\lambda$ with the wavelength $\lambda$. This random perturbation injects energy into all longitudinal spatial modes according to Reference [42] and should, therefore, reasonably approximate the case of a real mixing layer that is naturally submitted to a residual turbulence having a broadband spectrum. The small perturbation in the initial condition is expected to be amplified by so-called Kelvin–Helmholtz instabilities during the evolution of the flow. According to Reference [44], the most unstable wavelength $\lambda_a$ is given by $\lambda_a = 7\delta_0$, i.e. $\lambda_a = \frac{1}{4}$ in this case. The most amplified wavenumber is

$$\alpha_a = \frac{2\pi}{\lambda_a} = \frac{2\pi}{7\delta_0} = 8\pi \tag{52}$$

Thus, a number of $n_{\text{vort}}$ Kelvin–Helmholtz vortices is expected to develop in the streamwise direction for a domain with length $l_s = 7\delta_0 n_{\text{vort}}$ in this direction. With unit length chosen here, 4 vortices are supposed to appear. As may be observed in (51), a deterministic sine perturbation is also imposed. This results in fixing the position of the Kelvin–Helmholtz vortices on the $x_1$-axis. Otherwise, the vortices would take a randomly distributed position from one run to another, see Reference [42]. The sum of two waves with wavelength $\lambda_a = \frac{1}{4}$ and a smaller wavelength $\lambda_a = \frac{1}{10}$, respectively, are chosen according to Reference [43]. Consequently, the final velocity components including the perturbation are

$$u_{1,\text{per}}(x_2) = u_{1,\max}\left[\tanh\left(\frac{2x_2 - 1}{\delta_0}\right) + c_{\text{noise}}\frac{\partial \psi_{\text{per}}}{\partial x_2}\right] \tag{53}$$

and

$$u_{2,\text{per}}(x_2) = -u_{1,\max} c_{\text{noise}} \frac{\partial \psi_{\text{per}}}{\partial x_1} \tag{54}$$

 

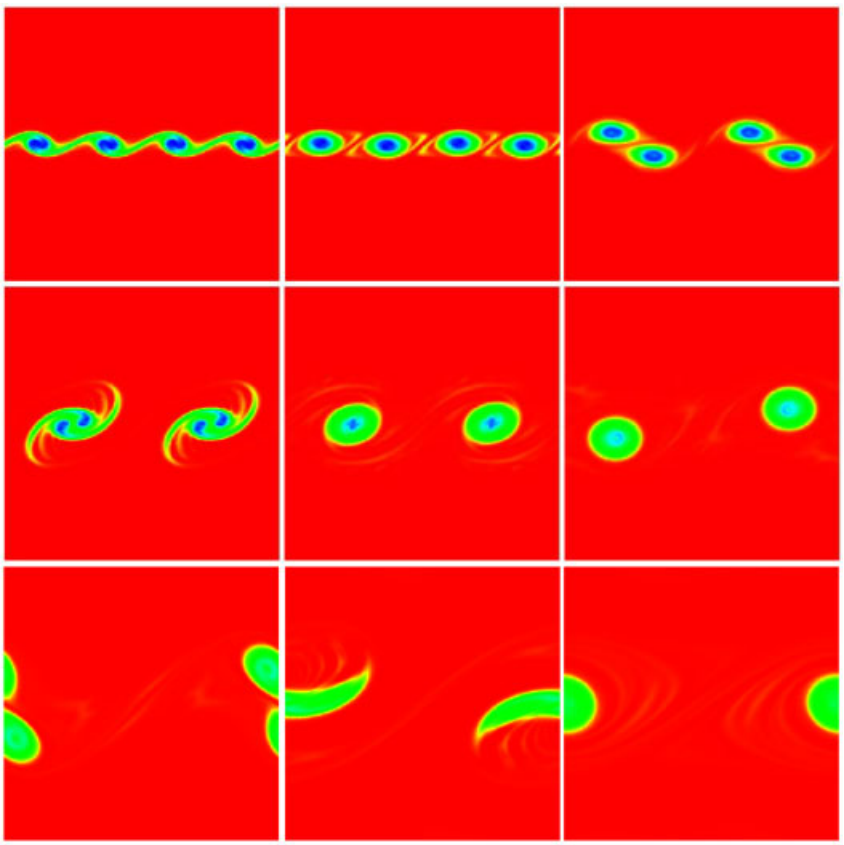

Figure 11. Coloured vorticity field (blue: intense vorticity, red: irrotational outer flow) at time units $10, 20, 30, 40, 70, 100, 110, 120, 200$ (left to right, top to bottom).

where $u_{1,\max}$ and $c_{\text{noise}}$ are specified to be 1 and $10^{-3}$, respectively. With these parameter specifications and a viscosity of $\nu = 3.571 \times 10^{-6}$, the Reynolds number of the problem amounts to be

$$Re = \frac{u_{1,\max}\delta_0}{\nu} = 10\,000 \tag{55}$$

Furthermore, a non-dimensional time unit, which is to be used later on, is defined as the actual time scaled by $\delta_0/u_{1,\max} = \frac{1}{28}$.

The physical evolution of the flow is explained via Figure 11. This picture series has been obtained from a simulation using the basic method, which will be described below, with $160 \times 160$ elements. The flow situations at non-dimensional time $10, 20, 30, 40, 70, 100, 110, 120,$ and 200 are displayed. Four different stages of this flow may be distinguished:

- *Development of four primary eddies*: The distinct appearance of the four primary eddies can be observed at about 15 time units. This corresponds to the point in time

 

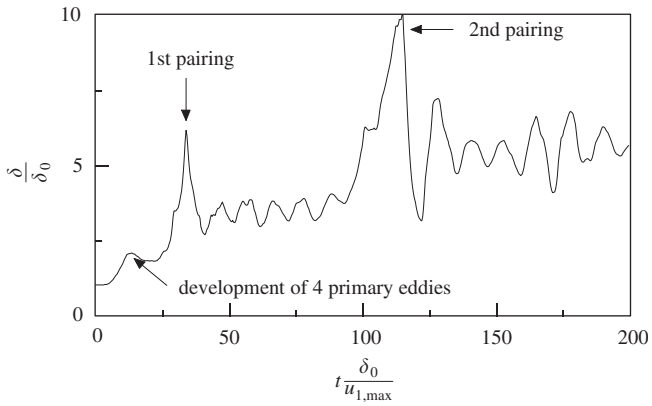


Figure 12. Principal sketch of the temporal evolution of the vorticity thickness (cf. Figure 11).

also observed in Reference [42] for the development to occur. John [45] found a later development at 30 time units.

- *First pairing*: The first pairing takes place at about 35 time units. Again, this compares exactly to the point in time noticed in Reference [42]. The later pairing in the simulation in Reference [45] at about 80 time units proceeded in a non-symmetric procedure, i.e. one pairing started earlier than the other. Here, both pairings occur at the same time.
- *Second pairing*: The second pairing is finished at about 115 time units. This is a later point in time in comparison to Reference [42] (75 time units) as well as an earlier one in comparison to Reference [45] (140 time units).
- *Rotation of the final vortex*: After the end of the second pairing, the final vortex rotates at a fixed position. The value of the vorticity thickness oscillates during this stage due to the elliptic shape of this vortex, confer Figure 12.

Four aspects of the flow are recorded quantitatively and displayed in Figures 13–16: the mean velocity $\langle u_1 \rangle$, the root-mean-square value of the velocity $u_1$, the total kinetic energy in the flow domain, and the vorticity thickness. The mean velocity $\langle u_1 \rangle$ at every node is evaluated as a discrete time average over the complete simulation time. In addition, these nodal values are spatially averaged over the periodic $x_1$ direction, in order to achieve a final velocity profile along the $x_2$ direction. The respective root-mean-square value is evaluated during the same averaging procedure. The total kinetic energy has already been defined in (49), and this definition is also applied in this example for the quantification of the temporal evolution of the energy. In principal, an evolution exhibiting a somehow decaying total amount of kinetic energy has to be expected, since the initial velocity distribution is subject to a non-zero viscosity, and no additional energy input is provided.

The scalar vorticity in the 2-D case is given as

$$\omega = \frac{1}{2}\left(\frac{\partial u_2}{\partial x_1} - \frac{\partial u_1}{\partial x_2}\right) \tag{56}$$

 

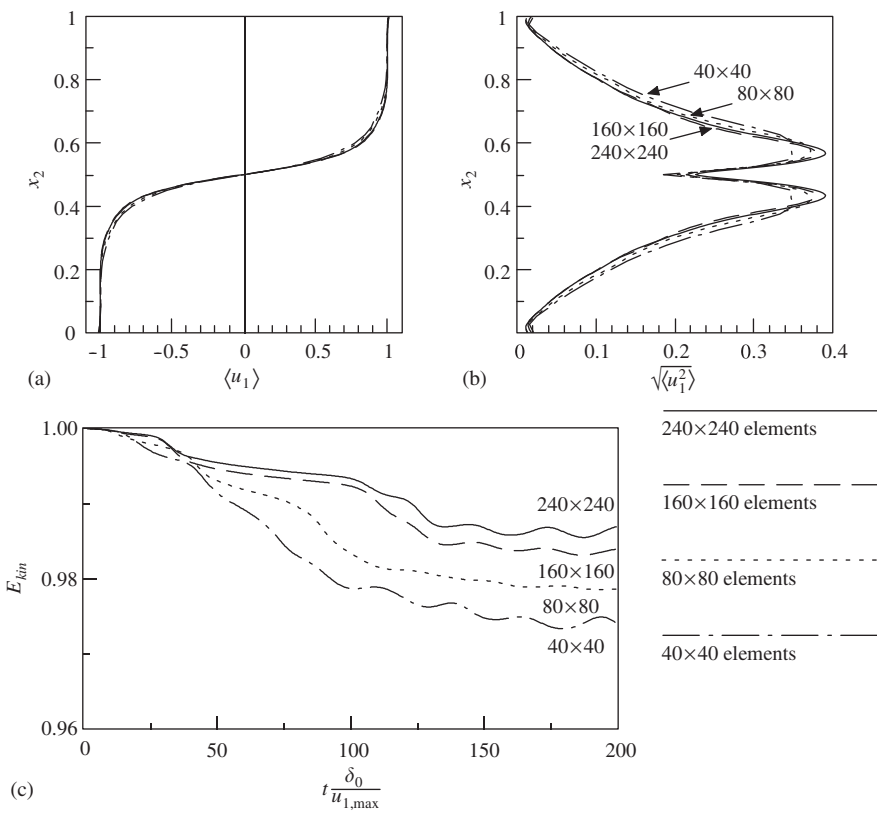


Figure 13. Various discretizations for the basic method: (a) mean velocities; (b) rms velocities; and (c) total kinetic energy.

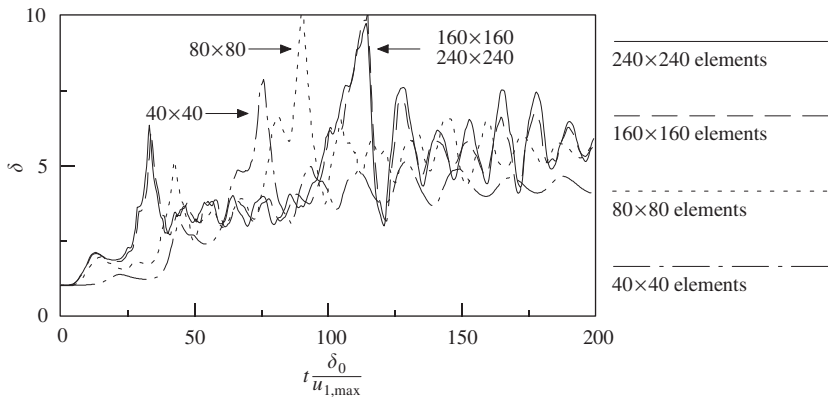


Figure 14. Various discretizations for the basic method: vorticity thickness.

 

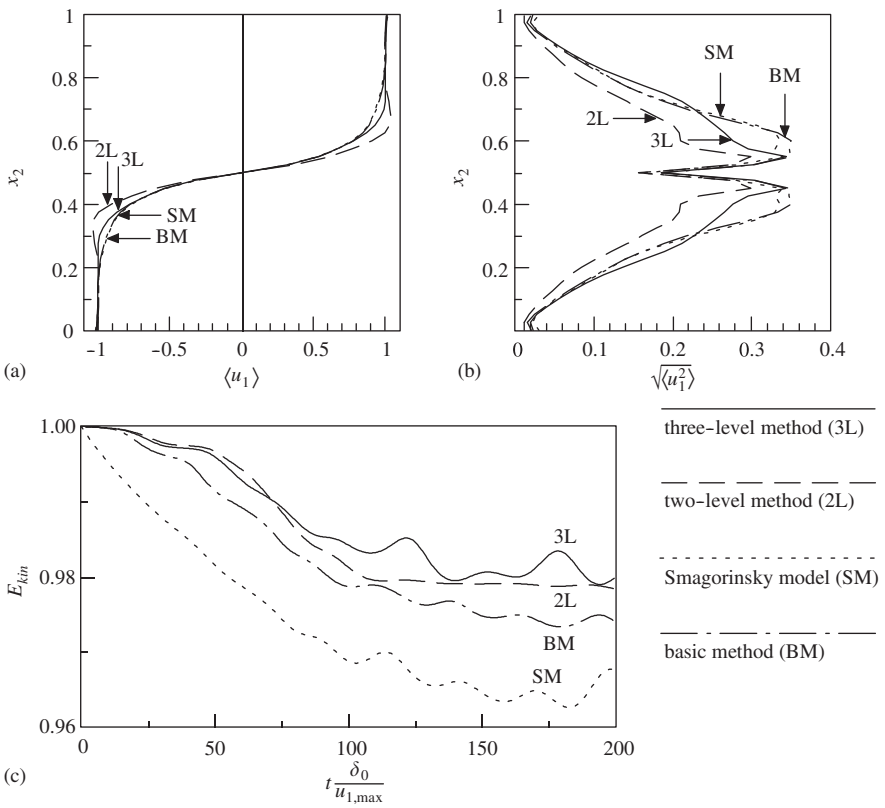


Figure 15. Various methods on a basic discretization with $40 \times 40$ elements: (a) mean velocities; (b) rms velocities; and (c) total kinetic energy.

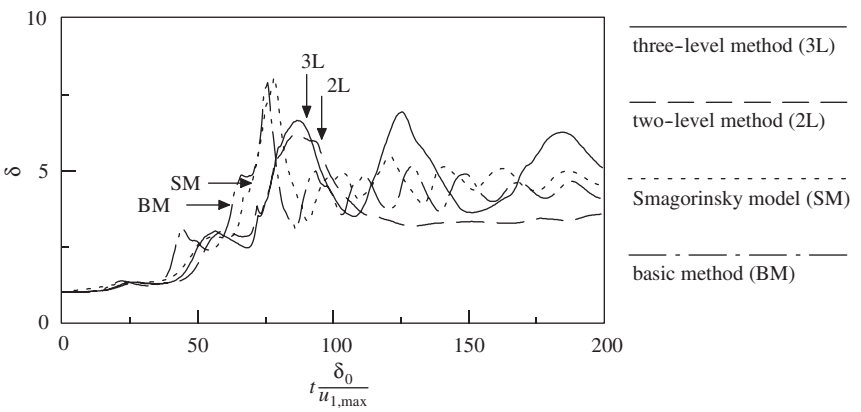


Figure 16. Various methods on a basic discretization with $40 \times 40$ elements: vorticity thickness.

 

The maximum value of $\omega$ may be defined as

$$\omega_{\max}(t) = \sup_{x_2 \in [0,1]} |\langle\omega\rangle(x_2,t)| \tag{57}$$

where $\langle\omega\rangle(x_2,t)$ denotes the integral mean in the periodic $x_1$ direction reading

$$\langle\omega\rangle(x_2,t) = \frac{\int_0^1 \omega(x_1,x_2,t)\,\mathrm{d}x_1}{\int_0^1 \mathrm{d}x_1} = \int_0^1 \omega(x_1,x_2,t)\,\mathrm{d}x_1 \tag{58}$$

In the practical computation, this integral is discretely evaluated for all mesh lines parallel to the $x_1$-axis according to Reference [45], and the maximum of these results is employed for $\omega_{\max}$. Based on this maximum value of $\omega$, the vorticity thickness $\delta$ is defined as

$$\delta(t) = \frac{\Delta u_{\mathrm{ml}}}{\omega_{\max}(t)} = \frac{2u_{1,\max}}{\omega_{\max}(t)} \tag{59}$$

with $\Delta u_{\mathrm{ml}}$ indicating the velocity jump across the mixing layer. The initial value for the vorticity thickness corresponding to the undisturbed velocity distribution is chosen to be $\delta(t=0) = \delta_0 = \frac{1}{28}$. All values $t > 0$ are scaled by this initial value $\delta_0$. A principal sketch of the temporal evolution is displayed in Figure 12 related to the calculation depicted in Figure 11. The particular stages of the respective flow, which have been characterized in the preceding section, may also be discovered in this course. The maximum values of the vorticity thickness at the first and second pairing are slightly higher than the comparable values in References [42, 45].

Basic discretizations with $40 \times 40$, $80 \times 80$, $160 \times 160$, and $240 \times 240$ bilinear quadrilateral elements of uniform length are chosen, respectively. This corresponds to 3280, 12 960, 51 520, and 115 680 velocity and 1639, 6479, 25 759, and 57 839 pressure degrees of freedom, respectively, related to the respective basic discretizations. The submeshes and the sub-submeshes are created with the same number of elements in each coordinate direction as in the previous example of the lid-driven cavity. Of course, this is restricted to two coordinate directions in the present 2-D case. With the $240 \times 240$ mesh, the resolution level of the quasi-DNS in Reference [42] is almost reached. Boersma *et al.* [43] applied local grid refinement up to this level only in the middle part of the flow domain, starting from an initial $80 \times 80$ discretization. The discretization in Reference [45] reached even further than the one in Reference [42] by using elements employing biquadratic velocity interpolation and discontinuous bilinear pressure interpolation for a DNS. This resolution level is comparable to $1024 \times 1024$ purely bilinear elements with respect to the number of velocity degrees of freedom, which is about 2 million. The number of pressure degrees of freedom, however, is considerably lower for this type of elements and resolution level in comparison to equal-order interpolated bilinear quadrilaterals.

Starting with the perturbed initial velocity field given in (53)–(54), the Crank–Nicolson scheme is used for the temporal discretization with a time step $\delta t = 0.35\delta_0/u_{1,\max} = 0.0125$. Overall, 570 time steps are performed, resulting in a simulation time of approximately 200 non-dimensional time units. Statistics are collected during the complete simulation time. Various methods are investigated. Firstly, a basic method is defined below. Secondly, the Smagorinsky model already used in the previous example is applied, i.e. the Smagorinsky

 

constant is again chosen to be $C_S = 0.1$. Thirdly, the two-level method as well as the three-level method with dynamic modelling are applied.

A first attempt to define a 'pure' PSPG finite element method as the basic method for the following investigations has failed even for the finest discretization with $240 \times 240$ elements. An immediate energy blow-up has been observed for this method, irrespective of the discretization. This is consistent with observations reported in the aforementioned literature dealing with this flow example. Even in Reference [42], a biharmonic dissipative term is added to the formulation applied on a $256 \times 256$ grid. (By the way, this explains the labelling 'quasi-DNS' for this simulation in Reference [42].) In Reference [43], a Smagorinsky term with $C_S = 0.1$ is added to the method which is applied on the finest grid with $240 \times 240$ grid points. In Reference [45], an energy blow-up is explicitly mentioned for a simulation without any additional dissipative term on a discretization level roughly comparable to a $128 \times 128$ mesh. According to the conclusion that it appears to be impossible to perform a DNS with the present discretizations, an additional dissipative term is incorporated into the PSPG finite element method. Deviating from the frequent use of the Smagorinsky model, an alternative in the form of a bulk viscosity term according to (42) is employed here. With this supplementary dissipative term, a reasonable basic method can be defined and is actually used in the following simulations.

In Figures 13 and 14, the results for simulations with the previously described basic method on various discretization levels are displayed. Figure 13(a) shows that the mean velocity profiles achieved with the various discretizations are fairly close together. The curves for the root-mean-values displayed in Figure 13(b) uncover the expected differences for the various resolution levels more distinctly. With regard to the temporal evolution of the total kinetic energy depicted in Figure 13(c), it is stated that the lower the resolution level, the higher the overall energy loss, i.e. the more dissipative is the method. An interesting observation may be made by analysing the temporal evolution of the vorticity thickness in Figure 14. The results for the $240 \times 240$ mesh and the $160 \times 160$ mesh almost coincide. However, the character of the curve is substantially modified for the coarser discretizations. In particular, it is observed that the coarser the discretization, the later the point in time indicating the first pairing, and, simultaneously, the sooner the second pairing. Furthermore, the actual values of the various amplitudes also appear to be quite different. It is concluded that the chosen discretization level has a considerable influence on the temporal development of the vorticity thickness and, hence, on the character of the flow.

The same conclusion is drawn for the investigation of various methods on the same resolution level instead of one method on various discretizations. The coarsest basic discretization with $40 \times 40$ elements is chosen for this purpose, in order to study the performance of the method under these less favourable circumstances, as already mentioned at the end of Section 5. Figure 16 shows the temporal evolution of the vorticity thickness for the aforementioned four methods. The basic method and the Smagorinsky model are fairly close together, which may be justified by their inherent similarity. Despite the small difference in the actual method, however, both curves may be precisely distinguished. The differences in comparison to the two- and three-level methods are evident, and also the differences between the two multi-level methods. In particular, the final stage of the simulated flow exhibits interesting varieties. The final vortex in the simulation using the basic method reveals a slightly elliptic character, confer also the last picture of the series in Figure 11 in this context. In contrast to this, the two-level method, on the one hand, produces an almost circularly shaped final

 

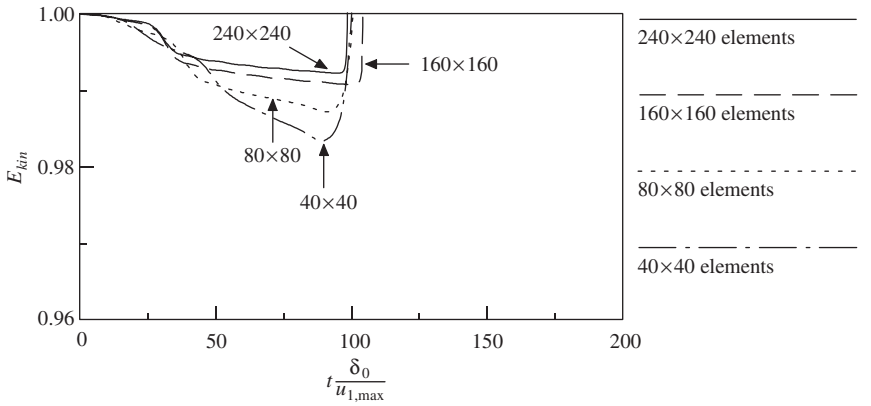


Figure 17. Evolution of the total kinetic energy for the USFEM on various discretizations.

vortex, and the three-level method, on the other hand, generates a more distinctly elliptic vortex at the end of the simulation. This is indicated by the amplitude of the oscillations in the temporal evolution of the vorticity thickness during the final stage of the flow. It is possible to verify with suitable calculations that this general tendency is not changed by using, for instance, a two-level method with a finer $8 \times 8$ submesh or a three-level method with various 'static' ways of modelling. After observing the velocity profiles in Figures 15(a) and (b), it is concluded that the two- level method fails to produce reasonable results at this Reynolds number. In particular, the overshoots in the left as well as the right section of the curve for the mean velocity in Figure 15(a) provide evidence for this conclusion. Finally, the temporal evolution of the energy depicted in Figure 15(c) indicates that the two- and the three-level method are less dissipative than the basic method, and the Smagorinsky model is the most dissipative of all methods, as expected.

A final remark should be made with regard to the stabilized method of USFEM-type for this particular flow example. There is a definite and fatal reason for the disregard of this method, see Figure 17. For every discretization under investigation, an energy blow-up has been observed, which starts approximately at the occurrence of the second pairing. Comparing the USFEM-type method to the basic method introduced before, it may be concluded that for the employed bilinear elements the only major difference between these two methods consists in the convective stabilization term, i.e. alternatively expressed, the classical SUPG-term, which introduces a certain amount of dissipation in the streamline direction. Further investigations have revealed that the zone of influence in which this energy blow-up emerges can be restricted to the vicinity of the upper and lower (free-slip) boundaries. More precisely, a sinusoidal perturbance with small amplitude on top of the actually constant velocity distribution of (absolute) unit value along the upper and lower boundary arises around the time of the second pairing. The amplitude is quickly amplified provoking the drastic energy blow-up in Figure 17 and causing the simulation to break down eventually. This issue is not pursued further, since the main focus of this work is not on stabilized methods. It is, however, interesting to note that this problem has not been observed for the two- and three-level method despite the close affinity between the USFEM and the multi-level finite element methods.

 

## 7. CONCLUSIONS

The variational multiscale method provides a methodical framework for the numerical simulation of turbulent flows. An important aspect of the particular implementations in this work, a two- and a three-level finite element method, is the use of residual-free bubbles with assumed zero Dirichlet boundary conditions on the element boundaries. This implementation guarantees the stability of the methods without further provisions and offers substantial computational savings on the small-scale level. Superior results with respect to an unusual stabilized finite element method (USFEM) have been obtained in the numerical flow examples of this work. On the contrary, however, the use of residual-free bubbles is also the reason for potential shortcomings of these methods, when coarse basic discretizations are used.

The multi-level methods are still open to improvement with regard to various aspects of the implementation. In particular, the dynamic procedure on the third level, which is initially based on some crude approximations, still invites to some further considerations. Even with substantial improvements, however, the aforementioned main drawback of the multi-level methods in this particular implementation remains and needs some further investigation, especially for the application to turbulent flows. Nevertheless, a somehow localized approach on the second level appears to be adequate for numerical simulations of turbulent flows. This is mainly due to perceptions of turbulence theory, which have shown that, for example, two-point correlations exhibit, in principal, a substantial significance only over a finite sector of the flow domain. The crucial measure in this context is the integral length scale and its relation to the length of the flow domain, both depending on the respective flow situation. The extreme localization procedure used in the present work, which resulted in a restriction of the permissible interaction of the small resolved scales to individual elements of a basic discretization, certainly exceeds the tolerable degree of localizing the small scales by far. However, a strategy ranging between this extreme localization, on the one hand, and a completely global concept demanding enormous computer resources, on the other hand, appears to be a very attractive future approach.

## REFERENCES

1. Sagaut P. *Large Eddy Simulation for Incompressible Flows* (2nd edn). Springer: Berlin, 2002.
2. Hughes TJR. Multiscale phenomena: Green's functions, the Dirichlet-to-Neumann formulation, subgrid scale models, bubbles and the origins of stabilized methods. *Computer Methods in Applied Mechanics and Engineering* 1995; **127**:387–401.
3. Hughes TJR, Stewart JR. A space-time formulation for multiscale phenomena. *Journal of Computational and Applied Mathematics* 1996; **74**:217–229.
4. Hughes TJR, Feijoo GR, Mazzei L, Quincy J-B. The variational multiscale method—a paradigm for computational mechanics. *Computer Methods in Applied Mechanics and Engineering* 1998; **166**:3–24.
5. Hughes TJR, Mazzei L, Jansen KE. Large eddy simulation and the variational multiscale method. *Computer and Visual Science* 2000; **3**:47–59.
6. Hughes TJR, Mazzei L, Oberai AA, Wray AA. The multiscale formulation of large eddy simulation: decay of homogeneous isotropic turbulence. *Physics of Fluids* 2001; **13**:505–512.
7. Hughes TJR, Oberai AA, Mazzei L. Large eddy simulation of turbulent channel flows by the variational multiscale method. *Physics of Fluids* 2001; **13**:1784–1799.
8. Collis SS. Monitoring unresolved scales in multiscale turbulence modelling. *Physics of Fluids* 2001; **13**: 1800–1806.
9. Gravemeier V, Wall WA, Ramm E. A three-level approach for incompressible Navier–Stokes. In *Proceedings of the Fifth World Congress on Computational Mechanics* (*WCCM V*), Mang HA, Rammerstorfer HG, Eberhardsteiner J (eds), Vienna, Austria, 7–12 July 2002, http://wccm.tuwien.ac.at
10. Guermond J-L. Stabilization of Galerkin approximations of transport equations by subgrid modelling. *Mathematical Modelling and Numerical Analysis* 1999; **33**:1293–1316.

 

11. Brezzi F, Fortin M. *Mixed and Hybrid Finite Element Methods*. Springer: New York, 1991.
12. Kaya S, Layton WJ. Subgrid-scale eddy viscosity methods are variational multiscale methods. *Technical Report TR-MATH 03-05*, Department of Mathematics, University of Pittsburgh, 2003.
13. John V, Kaya S. A finite element variational multiscale method for the Navier–Stokes equations. Preprint. *SIAM Journal on Scientific Computing*, 2004, in press.
14. Gravemeier V, Wall WA, Ramm E. A three-level finite element method for the instationary incompressible Navier–Stokes equations. *Computer Methods in Applied Mechanics and Engineering* 2004; **193**:1323–1366.
15. Germano M, Piomelli U, Moin P, Cabot WH. A dynamic subgrid-scale eddy vicosity model. *Physics of Fluids A* 1991; **3**:1760–1765.
16. Gresho PM, Sani RL. *Incompressible Flow and the Finite Element Method*: *Advection–Diffusion and Isothermal Laminar Flow*. Wiley: Chichester, 1998.
17. Gravemeier V. The variational multiscale method for laminar and turbulent incompressible flow. *Ph.D. Thesis*, *Report No. 40*, Institute of Structural Mechanics, University of Stuttgart, 2003 (http://www.uni-stuttgart.de/ibs/publications/phd/2000/fulltext/phdgravem.pdf).
18. Hughes TJR, Franca LP, Balestra M. A new finite element formulation for computational fluid dynamics: V. Circumventing the Babuska–Brezzi condition: a stable Petrov–Galerkin formulation of the Stokes problem accommodating equal-order interpolation. *Computer Methods in Applied Mechanics and Engineering* 1986; **59**: 85–99.
19. Wall WA. Fluid-Struktur-Interaktion mit stabilisierten Finiten Elementen (in German). *Ph.D. Thesis*, *Report No. 31*, Institute of Structural Mechanics, University of Stuttgart, 1999.
20. Smagorinsky J. General circulation experiments with the primitive equations. I. The basic experiment. *Monthly Weather Review* 1963; **91**:99–164.
21. Vreman A. The filtering analog of the variational multiscale method in large-eddy simulation. *Physics of Fluids* 2003; **15**:L61–L64.
22. Brezzi F, Russo A. Choosing bubbles for advection–diffusion problems. *Mathematical Models and Methods in Applied Sciences* 1994; **4**:571–587.
23. Franca LP, Farhat C. Bubble functions prompt unusual stabilized finite element methods. *Computer Methods in Applied Mechanics and Engineering* 1995; **123**:299–308.
24. Brezzi F, Franca LP, Hughes TJR, Russo A. $b = \int g$. *Computer Methods in Applied Mechanics and Engineering* 1997; **145**:329–339.
25. Brezzi F, Franca LP, Russo A. Further considerations on residual-free bubbles for advective–diffusive equations. *Computer Methods in Applied Mechanics and Engineering* 1998; **166**:25–33.
26. Franca LP, Farhat C, Lesoinne M, Russo A. Unusual stabilized finite element methods and residual free bubbles. *International Journal for Numerical Methods in Fluids* 1998; **27**:159–168.
27. Russo A. Bubble stabilization of finite element methods for the linearized incompressible Navier–Stokes equations. *Computer Methods in Applied Mechanics and Engineering* 1996; **132**:335–343.
28. Tezduyar TE, Osawa Y. Finite element stabilization parameters computed from element matrices and vectors. *Computer Methods in Applied Mechanics and Engineering* 2000; **190**:411–430.
29. Franca LP, Oliveira SP. Pressure bubbles stabilization features in the Stokes problem. *Computer Methods in Applied Mechanics and Engineering* 2003; **192**:1929–1937.
30. Codina R. Stabilized finite element approximation of transient incompressible flows using orthogonal subscales. *Computer Methods in Applied Mechanics and Engineering* 2002; **191**:4295–4321.
31. Franca LP, Macedo AP. A two-level finite element method and its application to the Helmholtz equation. *International Journal for Numerical Methods in Engineering* 1998; **43**:23–32.
32. Franca LP, Nesliturk A, Stynes M. On the stability of residual-free bubbles for convection–diffusion problems and their approximation by a two-level finite element method. *Computer Methods in Applied Mechanics and Engineering* 1998; **166**:35–49.
33. Franca LP, Nesliturk A. On a two-level finite element method for the incompressible Navier–Stokes equations. *International Journal for Numerical Methods in Engineering* 2001; **52**:433–453.
34. Nesliturk AI. Approximating the incompressible Navier Stokes equations using a two level finite element method. *Ph.D. Thesis*, University of Colorado, Denver, CO, 1999.
35. Brezzi F, Houston P, Marini D, Süli E. Modeling subgrid viscosity for advection–diffusion problems. *Computer Methods in Applied Mechanics and Engineering* 2000; **190**:1601–1610.
36. Prasad AK, Koseff JR. Reynolds number and end-wall effects on a lid-driven cavity flow. *Physics of Fluids A* 1989; **1**:208–218.
37. Zang Y, Street RL, Koseff JR. A dynamic mixed subgrid-scale model and its application to turbulent recirculating flows. *Physics of Fluids A* 1993; **5**:3186–3196.
38. Bardina J, Ferziger JH, Reynolds WC. Improved subgrid scale models for large eddy simulation. *AIAA Paper 80-1357*, 1980.
39. Ding X, Tsang TTH. Large eddy simulation of turbulent flows by a least-squares finite element method. *International Journal for Numerical Methods in Fluids* 2001; **37**:297–319.

 

40. Iliescu T, John V, Layton WJ, Matthies G, Tobiska L. A numerical study of a class of LES models. *International Journal of Computational Fluid Dynamics* 2003; **17**:75–85.
41. Franca LP, Valentin F. On an improved unusual stabilized finite element method for the advective–reactive–diffusive equation. *Computer Methods in Applied Mechanics and Engineering* 2000; **190**:1785–1800.
42. Lesieur M, Staquet C, LeRoy P, Comte P. The mixing layer and its coherence examined from the point of view of two-dimensional turbulence. *Journal of Fluid Mechanics* 1988; **192**:511–534.
43. Boersma BJ, Kooper MN, Nieuwstadt FTM, Wesseling P. Local grid refinement in large-eddy simulations. *Journal of Engineering Mathematics* 1997; **32**:161–175.
44. Michalke A. On the inviscid instability of the hyperbolic tangent velocity profile. *Journal of Fluid Mechanics* 1964; **19**:543–556.
45. John V. Large eddy simulation of turbulent incompressible flows. *Analytical and Numerical Results for a Class of LES Models*. Springer: Berlin, 2004.

 